AN ABSTRACT OF THE THESIS OF

Sjamsie Husurianto for the degree of Master of Science in Chemical Engineering presented on June 18, 1998. Title: Process Optimization and Electrical Characterization of ZnS:Mn Electroluminescent Phosphors Deposited by Halide Transport Chemical Vapor Deposition.

Abstract approved: Redacted for Privacy

Milo D. Koretsky

Process development of halide transport chemical vapor deposited (HTCVD) ZnS:Mn thin film has been studied. To this end, electrical characterization of HTCVD ZnS:Mn electroluminescent devices has been used. Process optimization focused on a simple design of experiment (DOE) with brightness as the major response.

Deposition parameters such as HCl and H_2S gas flow rates, ZnS and Mn source temperatures and substrate temperature were studied. A substrate temperature of 550 ^{o}C gives the brightest devices. ZnS source temperature and H_2S gas flow rate are insignificant parameters according to the statistical analysis. However HCl gas flow rate and Mn source temperature show strong interaction. It is proposed that the incorporation of Cl into the ZnS:Mn film causes the interaction. A Cl defect is also consistent with anomalous electrical behavior observed in the devices. Cl defects are thought to precipitate at the grain boundaries of the initial growth interface, then diffuse (or migrate) along the grain boundaries and possibly into the bulk crystal. This

defect will easily form negative charge leading to asymmetric space charge in the bulk of the phosphor.

Since the defects are believed to originate from the nucleation of Cl at high grain boundary density, one potential solution is to remove the Cl source as the grains begin to grow and only later expose the film to Cl. While film growth without HCl present at the beginning of deposition leads to brighter films, it is a sub-optimal solution. Part of the ZnS host does not have luminescent centers. It is believed other processing solutions need to be realized to make the HTCVD system viable.

Process Optimization and Electrical Characterization of ZnS:Mn Electroluminescent Phosphors Deposited By Halide Transport Chemical Vapor Deposition

by

Sjamsie Husurianto

A THESIS

submitted to

Oregon State University

in partial fulfillment of
the requirements for the
degree of

Master of Science

Completed June 18, 1998
Commencement June 1999

Master of Science thesis of Sjamsie Husurianto presented on June 18, 1998

APPROVED:

Redacted for Privacy

Major Professor, representing Chemical Engineering

Redacted for Privacy

Head of Department of Chemical Engineering

Redacted for Privacy

Dean of Graduate School

I understand that my thesis will become part of the permanent collection of Oregon State University libraries. My signature below authorizes release of my thesis to any reader upon request.

Redacted for Privacy

Sjamsie Husurianto, Author

ACKNOWLEDGMENT

This thesis could not be done and completed without the help and support of many others. Particularly, I would like to express my appreciation to:

Dr. Milo Koretsky for his great idea, patience, guidance, and support throughout my graduate studies in Oregon State University.

Dr. John F. Wager and Dr. Thomas K. Plant for the use of their research facilities.

Paul Keir for his help with the PECVD system and for sharing his expertise in ZnS:Mn phosphors.

Chia-Chang (Kevin) Hsu and Amadou Camara for their advise, assistance in the lab and friendship.

P. Nick Wannemacher for his technical assistance.

The rest of the Koretsky and Wager research groups for their help.

Lastly, I would like to thank my family, especially my parents who were willing to sacrifice for the success of their son and my wife for all her patience, support and encouragement.

This work was supported by the Advanced Research Project Agency under the Phosphor Technology Center of Excellence, Grant Number MDA 972-93-1-0300.

TABLE OF CONTENTS

Page

TABLE OF CONTENTS (CONTINUED)

Page

LIST OF FIGURES

LIST OF FIGURES (Continued)

Figure Page

LIST OF FIGURES (Continued)

LIST OF TABLES

dedicated to
my wife and parents

PROCESS OPTIMIZATION AND ELECTRICAL CHARACTERIZATION OF ZnS:Mn ELECTROLUMENESCENT PHOSPHORS DEPOSITED BY HALIDE TRANSPORT CHEMICAL VAPOR DEPOSITION

Chapter 1

INTRODUCTION

Today, the flat panel display industry is dominated by liquid crystal displays (LCD). However there are a few shortcomings associated with LCDs, such as limited viewing angle and the requirement of an external light source. Alternative flat panel display technologies include plasma, field emission (FED), and electroluminescent (EL) displays. Each of these displays has its own advantages and disadvantages.

EL displays are a promising candidate for replacing the LCD. There are four types of EL displays: alternating-current (AC) thin film EL (ACTFEL), AC powder EL, direct-current (DC) thin film EL, and DC powder EL. Among these, ACTFEL displays are currently the best for commercial application due to their long lifetime and durability.

ACTFEL displays offer many advantages when compared to LCDs, such as higher brightness, higher contrast, wider viewing angle, faster response time, and improved thermal and mechanical stability. Also, because it is a self-illuminating device, ACTFEL displays do not require an external light source. Even though ACTFEL displays have better characteristics than LCD, there are a few crucial obstacles to mass production of full size and full color ACTFEL displays. Development of a stable, bright blue phosphor for full color displays has been elusive. The second obstacle is the difficulty in mass producing uniform and high quality ACTFEL displays over large areas especially for displays 14 inches or larger diagonal.

Processing throughput, cost and uniformity are very important to make ACTFEL displays commercially viable.

Light in an ACTFEL device is emitted from group a II-VI compound phosphor via electron impact excitation of luminescent centers. The excited luminescent centers then decay emitting light. The most common phosphor host materials are ZnS, ZnSe, CaS, SrS, and SrSe. Mn, Ce and other rare earth and lanthanide ions are used as the luminescent centers. In this study, ZnS doped with Mn is used.

The focus of this thesis is on process optimization of ZnS:Mn deposition using halide transport chemical vapor deposition (HTCVD) and on electrical characterizations of HTCVD ZnS:Mn ACTFEL devices. HTCVD is believed to be able to produce films with large crystal grains, bright luminescence and excellent aging stability. HTCVD also provides low-cost and large area deposition capability. The process optimization is done through a simple design of experiment (DOE) with brightness of ACTFEL device as the response. Results of electrical characterizations are also used in the process characterization and optimization.

The thesis is organized as follows: Chapter 2 is a review of the literature of previous work on ZnS:Mn ACTFEL devices, including device fabrication, physics of device operation, device modeling and phosphor space charge in ZnS:Mn ACTFEL devices. Chapter 2 also presents a fundamental model to understand the electrical characteristics of an ideal ZnS:Mn ACTFEL device. In Chapter 3, experimental techniques employed in this study are discussed. These include fabrication of HTCVD ZnS:Mn ACTFEL devices, different techniques of electrical characterization and the DOE of HTCVD ZnS:Mn deposition. Chapter 4 discusses the results of process optimization of HTCVD ZnS:Mn deposition and of electrical characterizations. The final chapter, Chapter 5 presents the conclusions of this study.

Chapter 2

LITERATURE REVIEW OF ZnS:Mn ACTFEL DEVICES

2.1 Brief History

Light emission from a phosphor powder was first observed in the early 1930's. In 1936, Destriau [1936] obtained emission of light by applying a large AC potential to a ZnS phosphor powder dispersed in an insulator and sandwiched between two electrodes. The first ZnS:Mn thin-film electroluminescent (EL) device was developed by Vlasenko [1960] in the late 1950's using a transparent conductive film (SnO_2). Russ and Kennedy [1967] developed the double-insulating layer structure which improved the lifetime and luminance of EL devices. At the 1974 SID (Society on Information Display) International Symposium, Inoguchi *et al.* [1974] reported a stable, long life (> 10,000 hours of operation), high luminance (~3400 cd/m^2, at 5 kHz) orange-yellow-emitting ZnS:Mn thin film EL panel with the double-insulating layer structure. In 1983, the first commercial production of 6 inch-diagonal matrix monochrome ZnS:Mn EL display was introduced [Takeda *et al*,1983].

Since then, extensive research has been focused on developing full-color AC-driven thin-film electroluminescent (ACTFEL) displays. The first commercial full-color EL display, based on the inverted, patterned color filter EL device structure, was first produced and marketed in 1994 [Barrow, 1994].

2.2 ACTFEL Device Structure

A typical double-insulating layer ZnS:Mn ACTFEL device structure is shown in Figure 2-1. The ZnS:Mn phosphor film is sandwiched between two insulators and a pair of electrodes. The bottom electrode is made of indium tin oxide (ITO). ITO is transparent to visible light and is a conductor of electricity. Aluminum titanium oxide (ATO) and silicon oxynitride (SiO_xN_y, SiON) are used for the bottom and top insulating layers, respectively. Both ATO and SiON are also transparent to visible light and have relatively high dielectric constant (ε_r=11.5 and 6.0, respectively) which protect the phosphor layer from electrical breakdown. For the top electrode, aluminum is used because it has a good adhesiveness to the top insulating layer. It also has no metal-ion migration at high electric fields and an ability to prevent breakdown spread when dielectric breakdown of the phosphor layer or insulating layer occurs. All these films are grown on top of Corning 7059 glass substrate. Other insulating materials, such as yttrium oxide (Y_2O_3), barium tantalite ($BaTa_2O_6$, BTO), and, silicon nitride (Si_3N_4), also have been used [Ono, 1995].

The phosphor layer consists of zinc sulfide host material doped with manganese luminescent centers (ZnS:Mn, a II-VI semiconductor compound). ZnS:Mn emits yellowish-orange light with a peak intensity around 585nm when excited by a high electric field. Many other II-VI compounds, such as ZnSe, CaS, SrS, and SrSe, serve as hosts for EL phosphors.

2.3 ZnS:Mn ACTFEL Device Fabrication

The fabrication of ZnS:Mn ACTFEL device involves several processing steps. The device fabrication starts from the growth of ITO, as bottom electrode, on top of a Corning 7059 glass substrate. This process is usually done by sputtering. The bottom insulator, ATO, is then laid down on top of ITO, also by sputtering. The next step,

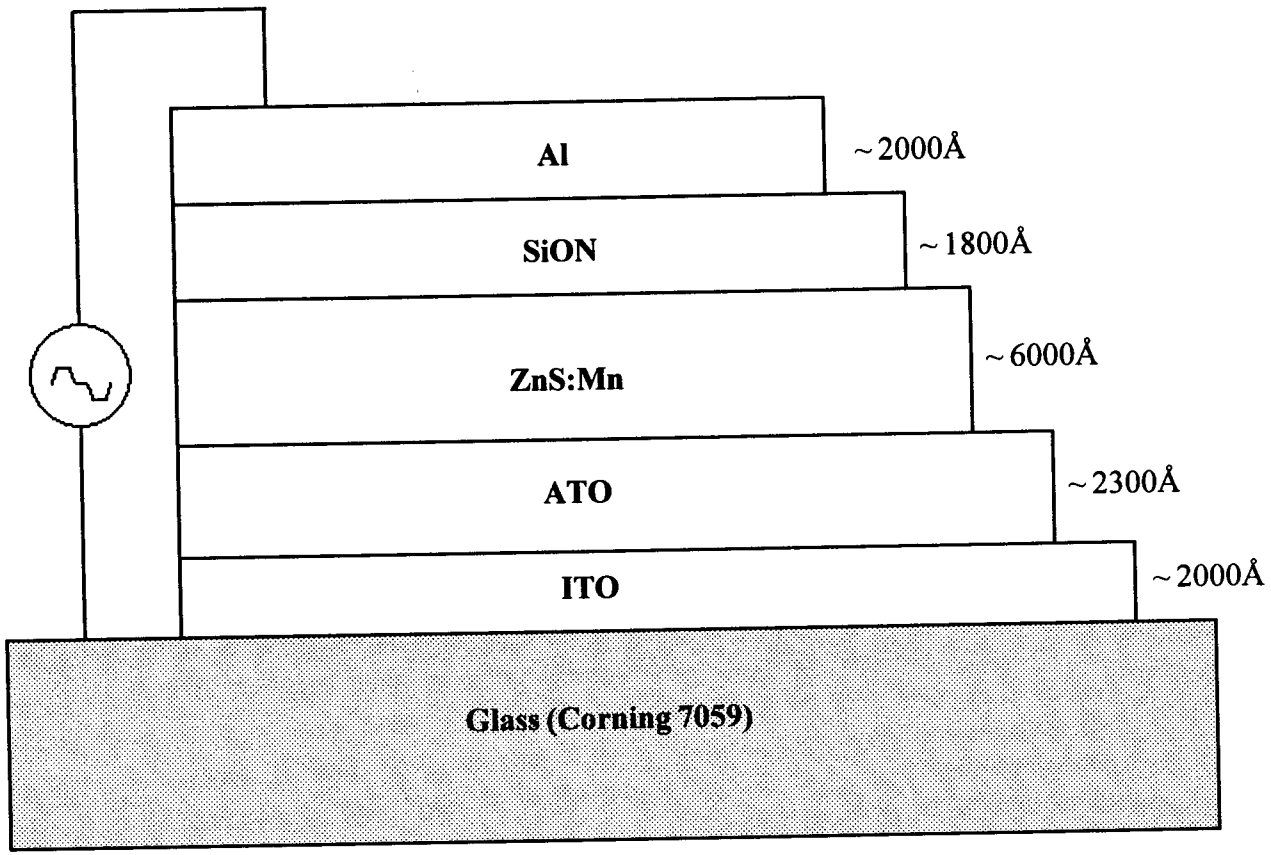

Figure 2-1. ZnS:Mn ACTFEL device structure.

consists of depositing the heart of ACTFEL device, the phosphor. The phosphor thin film can be processed either by physical vapor deposition (PVD) such as: electron beam evaporation (EBE) [Hurd, 1979; Ono, 1995], multi-source deposition (MSD) [Nire, 1994], sputtering [Xian, 1994], and thermal evaporation [Ono, 1995], or by chemical vapor deposition (CVD) techniques such as: metal-organic chemical vapor deposition (MOCVD) [Migita, 1988], halide transport chemical vapor deposition (HTCVD) [Mikami, 1991; Chen *et al*, 1998], and atomic layer epitaxy (ALE) [Suntola, 1992]. Physical vapor deposition provides a higher deposition rate and requires a lower substrate temperature while chemical vapor deposition results in films with better crystallinity and higher luminous efficiency. The deposition of the top insulator layer, SiON, usually is done by plasma enhanced chemical vapor deposition (PECVD). To complete ACTFEL device fabrication, aluminum dots are deposited on top of the SiON film using evaporation.

So far, ZnS:Mn thin films have been produced commercially by EBE and ALE. ALE produces films with good crystal quality, large grain size (>100 nm) and columnar grain growth, but it is expensive and requires a long deposition time. EBE has a lower start-up and operational cost than ALE, but it produces films with smaller grains (25 nm) [Ono, 1995; Theis, 1983], although post-deposition thermal annealing can improve the grain size and enhance the film crystallinity.

HTCVD is potentially well suited as an alternative to ALE. Its low-cost, large-area deposition capability, and its ability to produce films with crystal grains as large as 100 nm [Chen, 1998], bright luminescence, and excellent aging stability [Mikami, 1992] is very attractive. All the phosphor films used in this study are deposited using HTCVD.

The molecular processes during ZnS:Mn film growth by HTCVD are illustrated in Figure 2-2. ZnS powder is heated to 900 - 980 ^{o}C, sublimates and is carried to the

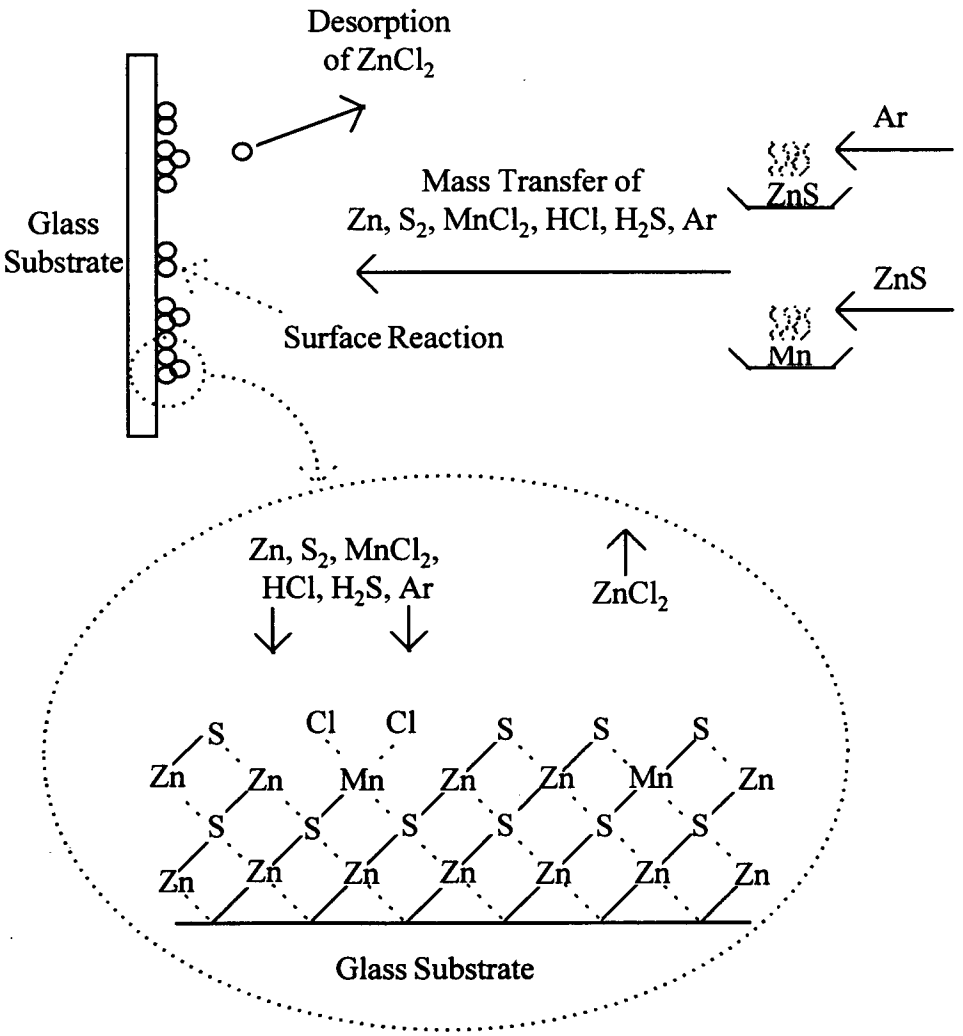

Figure 2-2. ZnS:Mn deposition process in HTCVD system.

reaction chamber by a carrier gas (either H_2 or Ar). Mn enters the reaction chamber as $MnCl_2$ by passing HCl over a heated (725 - 775 °C) metallic Mn source. The chemical reactions of ZnS and Mn powders in these heaters are given by:

$$2\ ZnS\ (s) \longrightarrow 2\ Zn\ (g) + S_2\ (g) \qquad (2\text{-}1)$$

$$Mn\ (s) + 2\ HCl\ (g) \longrightarrow MnCl_2\ (g) + H_2\ (g). \qquad (2\text{-}2)$$

The gas species, Zn, S_2, $MnCl_2$, and H_2, then mix and transport to the substrate surface simultaneously for deposition. S_2 absorbs and dissociates into S and, along with Zn, will diffuse along the growing film surface until it finds a low energy site and is incorporated into the film. At the same time, $MnCl_2$ will disociatively chemisorb on the surface. The Cl atoms will react with a Zn atom to form $ZnCl_2$, which is volatile and can desorb from the surface while the Mn luminescent centers are incorporated in the film.

The ZnS:Mn film growth rate depends on substrate temperature [Mikami *et al.*, 1991]. The growth rate increases as the substrate temperature increases and reaches a maximum at 550 °C. Above 550 °C the growth rate decreases very sharply. The growth is reaction limited below 500 °C. Between 500 and 550 °C, the growth shifts from reaction controlled to mass-transfer controlled. One explanation of the rapid decrease of the growth rate above 550 °C is because of a deficiency of the source vapors diffusing to growing surface. Mikami *et al.* [1991] reported that at substrate temperatures above 600 °C, small irregular particles are observed in the deposited film. The particles, generated by homogeneous reaction in gas phase, reduce reactants available for thin film growth from the system.

2.4 Physics of ZnS:Mn ACTFEL Device Operation

The ACTFEL device is operated by applying a large AC voltage across the electrodes. In a commercial matrix-addressed configuration flat panel display, a voltage just below the threshold voltage is applied to the row electrodes while another voltage pulse is applied to the column electrodes resulting a total voltage across the device exceeding the threshold voltage which results in the emission of light. Ono defines the threshold voltage as the voltage corresponding to a luminance of 1 cd/m^2 [Ono, 1995]. ACTFEL devices are typically operated at 40 V above the threshold voltage.

In this study, an alternating bipolar trapezoidal voltage pulse is used. The voltage waveform is shown in Figure 2-3. It has 5 μs rise and fall times and a pulse width of 30 μs. The frequency of the waveform is 1 kHz. The applied amplitudes of the waveform are typically 20, 40 and 60 V above the threshold voltage. Other waveforms such as sinewaves and triangular (sawtooth) waveforms have been used by other researchers.

The basic mechanism of EL emission can be explained as follows. When the applied bias is below the threshold voltage, electrons remain at the insulator-phosphor interface. At the threshold voltage, the phosphor layer breaks down. At this point, electrons are injected into the phosphor from interface states. As the electrons transport through the phosphor layer, they are accelerated by the applied field and gain kinetic energy. Electrons with sufficiently high energy, also know as hot-electrons, will excite the bound electrons in the luminescent centers upon impact. EL emission is realized when an excited electron in a luminescent center makes a radiative transition to the ground state.

A better picture of ACTFEL device operation can be obtained by using energy band diagrams of the device during various portions of the driving waveform. An ideal

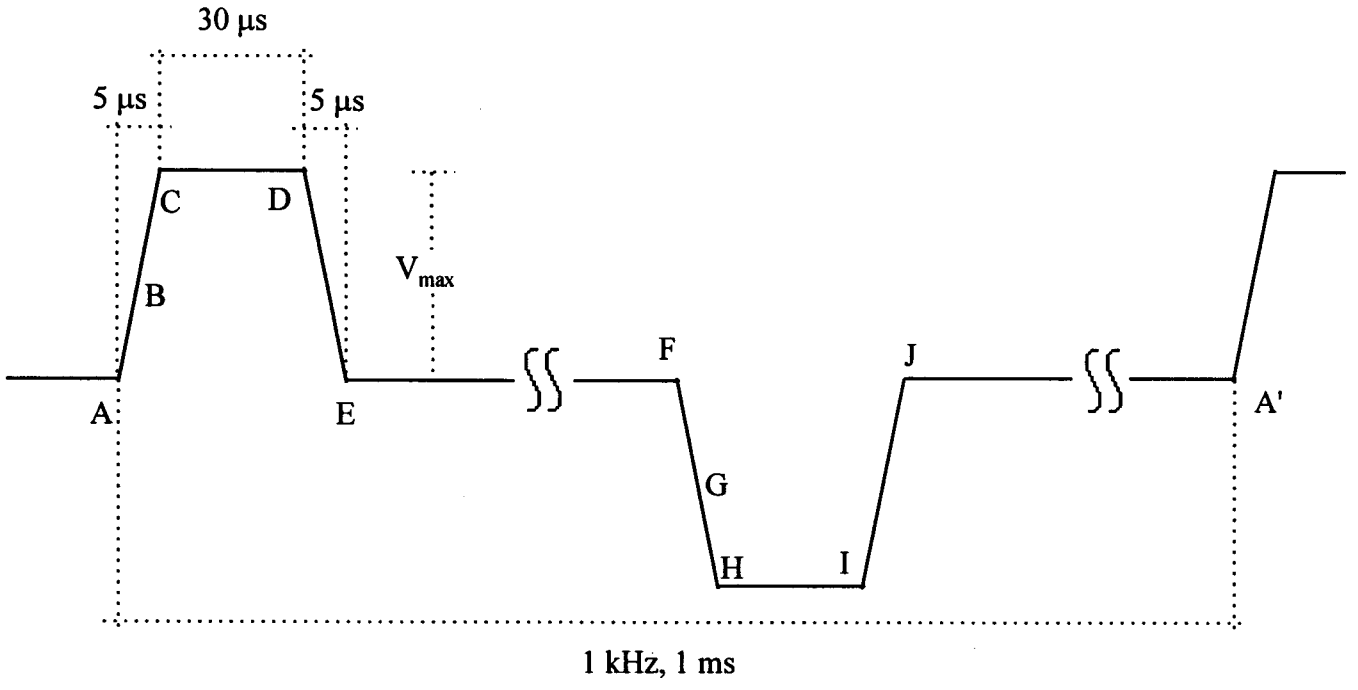

Figure 2-3. Applied voltage waveform for ACTFEL device analysis.

ACFTEL device's energy band diagram in equilibrium, when no external bias applied to the device, is shown in Figure 2-4 (a) [Douglas, 1993].

Figure 2-4 (b) shows the shape of energy band diagram when the first voltage pulse is applied to the ACTFEL device. At this time, a positive bias, V_{appl}, is applied to the Al electrode as shown in the figure. The voltage drop across the two insulating layers and the phosphor layer is divided according to their capacitance. The capacitance of each layer is determined by its dielectric constant and thickness. When the electric field across the phosphor reaches its critical value, corresponding to the external threshold voltage, trapped electrons at the insulator-phosphor interface on the cathodic side tunnel out into the phosphor layer conduction band. The emitted electrons are accelerated by the phosphor electrical field towards the opposite interface. This pulse of current dissipates real power and is known as conduction current. If the accelerated electrons gain enough energy before they reach the opposite interface, they may impact excite a luminescent center. For Mn excitation, an energy of 2.1 eV is required to excite electrons in the Mn luminescent centers from the $3d^5$ ground state to the local excited states. Emission of photons (light) can be realized when the excited electrons decay back to their ground states. For Mn doped ZnS, the emitted light is orange-yellow in color (centered at 585 nm).

During this pulse, positive charge builds up on the cathodic interfaces as electrons are injected into phosphor layer. Meanwhile, negative charge accumulates on the opposite anodic interface as the electrons tunneling from the cathodic interface are collected. When the external applied voltage is terminated (zero), both charges still remain at their respective interfaces, as shown in Figure 2-4 (c). The absolute value of the charge is called the polarization charge, Q_{pol}. Polarization charge gives rise to a phosphor field component that discourages the additional injection of electrons. Although there is no externally applied voltage across the device, there are still internal

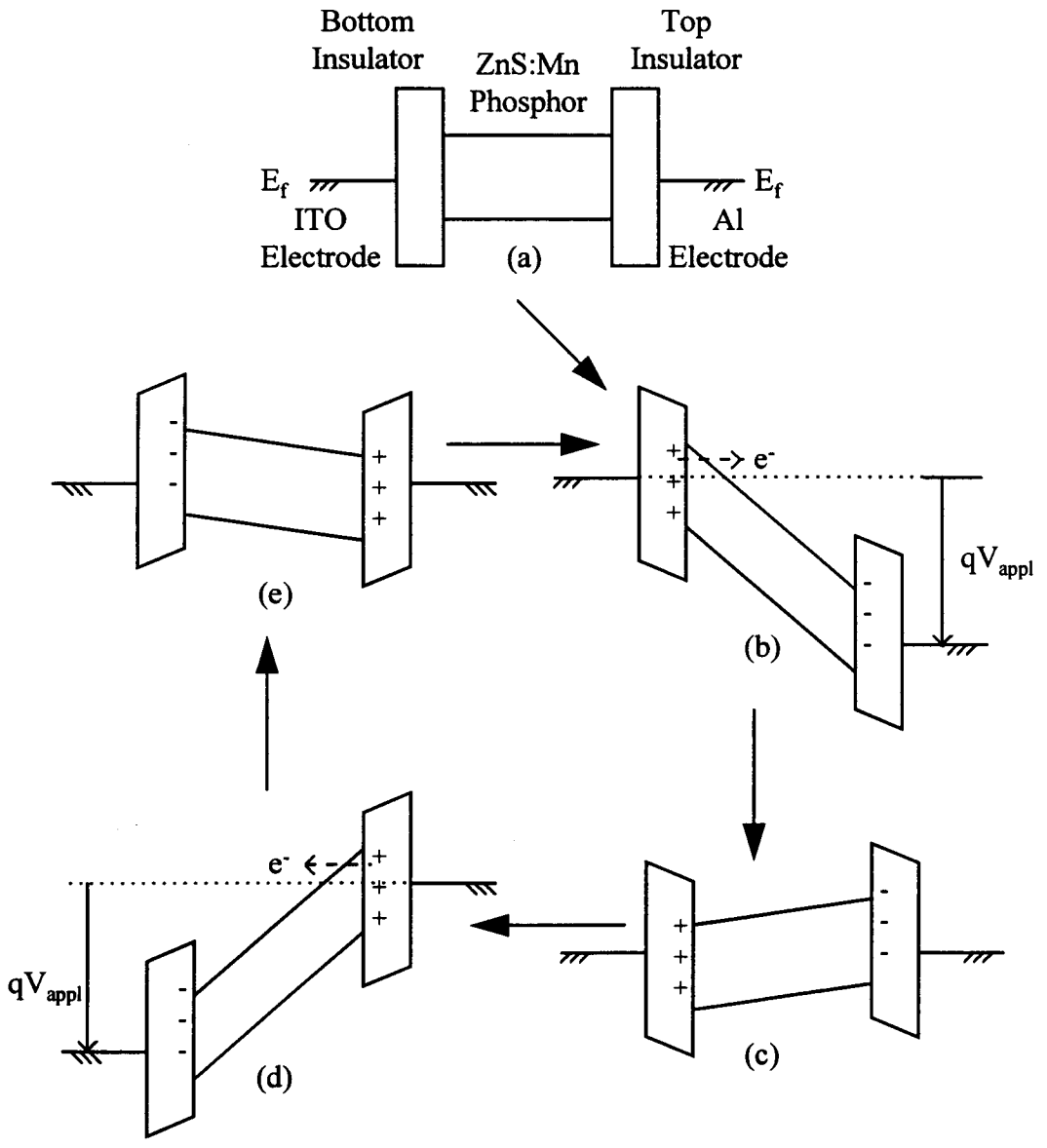

Figure 2-4. Cycle of energy band diagrams.

fields in the device due to the net charge at the phosphor-insulator interfaces. This internal field is called the residual polarization field [Brienguier, 1989]. In some cases, it is strong enough to cause emission of some electrons from the interface with negative charge. The charge emitted during this period due to the residual polarization field is called leaked charge, Q_{leak}, because these electrons are no longer available for tunneling when the next opposite polarity pulse arrives.

Figure 2-4 (d) shows the energy band diagram when the opposite voltage pulse (negative) is applied to the device. Now, the conduction current flows in the opposite direction with respect to Figure 2-4 (b). During this voltage pulse, the polarity of the polarization charge assists the emission of electrons and lowers the threshold voltage. However, after a sufficient number of electrons have tunneled from the cathodic interface, the charge on the cathodic interface changes sign and the internal field opposes the applied field as before.

When the negative pulse ends, the same basic phenomena that occurred after the end of the positive pulse manifest. Figure 2-4 (e) shows the energy band diagram which is just a mirror image of the energy band diagram in Figure 2-4 (c). This energy band diagram cycle continues as subsequent voltage pulses are applied to the ACTFEL device. Electrons in luminescent centers are continuously excited during the portion of cycle in which conduction occurs and light is emitted as those excited electrons in luminescent centers decay to their ground states. This process reaches steady state in about 2 or 3 cycles.

2.5 ACTFEL Device Modeling

A simple equivalent-circuit model of a double-insulating layer ACTFEL device is shown in Figure 2-5. This circuit model was introduced by Smith [1981]. C_{it} and C_{ib} are the capacitances of the top and bottom insulator layers, respectively. C_p is the phosphor capacitance. The phosphor capacitance is shunted by two back-to-back zener diodes. The breakdown voltage of these zener diodes is set to the threshold voltage for the onset of conduction across the phosphor. The phosphor capacitance is shorted during conduction. This is the model that will be used later to estimate the physical insulator and physical phosphor capacitance of an ACTFEL device.

The physical insulator capacitance (C_i) and total capacitance (C_t) are calculated using the following equations,

$$\frac{1}{C_i} = \frac{1}{C_{it}} + \frac{1}{C_{ib}}, \tag{2-3}$$

$$\frac{1}{C_t} = \frac{1}{C_i} + \frac{1}{C_p}. \tag{2-4}$$

More sophisticated and complex ACTFEL device equivalent circuit models have been proposed (for example, Davidson *et al* [1992], Singh [1992], Keir et *al* [1995], Ylilammi [1995]). Keir's models include the effect of space charge generation due to field emission from bulk traps or impact ionization of deep-level traps.

2.6 Phosphor Space Charge

Anomalous ZnS:Mn ACTFEL device behavior has been linked to the presence of space charge in the phosphor layer of the device. Phenomena such as brightness-voltage (B-V) hysteresis, negative differential resistance, internal charge-phosphor field ($Q\text{-}F_p$) overshoot, and capacitance-voltage (C-V) overshoot can be all explained by

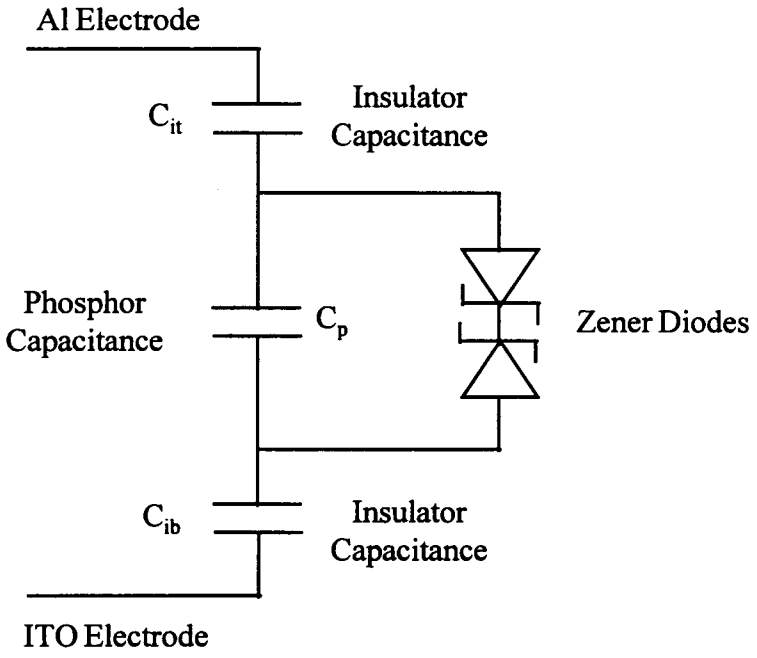

Figure 2-5. Simple ACTFEL device equivalent circuit model.

space charge [Keir, 1995]. A detail explanation of B-V, Q-F_p, and C-V will be given in Section 2.7 and Chapter 3.

The presence of space charge in the phosphor layer causes a distortion of the electric field. Instead of a constant field across the phosphor layer, now it varies according to time and position in the phosphor layer. If one interface experiences an increased electric field relative to the other interface, the conducted charge may be asymmetrical. Furthermore, if the space charge is positive, the field near the emitting interface is increased and a catastrophic breakdown of the phosphor layer may occur.

The mechanism of space charge generation has been postulated by many researchers, but so far there is no definitive proof of the generation process. The proposed generation processes include impact ionization, field ionization, hole capture, electron hole pair generation, and Auger processes. The most common explanation of space charge generation in the literature is that it is created by trapped holes which are generated by band-to-band impact ionization processes [Howard, 1982; Jarem, 1988; Neyts, 1994; Goldenblum, 1994]. But, Yang *et al* [1983] suggest, because of energy considerations, space charge is more likely created by impact ionization of deep-level traps than by trapped holes. It is not clear what exactly is causing space charge in the phosphor layer.

2.7 Electrical Characteristics of an Ideal ZnS:Mn ACTFEL Device

Since a significant fraction of the data in this thesis relates to electrical characterization of HTVCD ZnS:Mn ACTFEL devices, a brief, fundamental description of the electrical properties of a typical device is presented. This discussion will serve to introduce some of the terminology and phenomena that will be presented later. It should be noted that the description below relates to an ideal device/system.

Table 2-1 (a). Physical characteristics of the dielectric layers of a typical ACTFEL device.

Film	Capacitance (nF/cm^2)	Thickness (μm)
ATO	48.7	0.23
ZnS:Mn	12.1	0.60
SiON	27.5	0.18
Total	7.17	1.01

Table 2-1 (b). Electrical characteristics of a typical ACTFEL device.

V_{th}	100 V
Q_{pol}	0.7 $\mu C/cm^2$
V_{max}	160 V

The geometry of the system is shown in Figure 2-1. The ITO electrode is grounded and a voltage pulse as shown in Figure 2-3 is applied to Al electrode. This system can be modeled as three dielectrics in series: ATO, ZnS:Mn, SiON. Important physical properties of the dielectric films are given in Table 2-1 (a). These values are characteristic of the devices used in this study. Similarly, values representative of a typical ACTFEL device are given in Table 2-1 (b), where V_{th}, Q_{pol}, and V_{max} are the threshold voltage, polarization charge, and maximum applied voltage respectively. We will base the discussion in this section on the values reported in Tables 2-1.

We consider two principle components which affect the electrical behavior of the device:

1. the external applied potential, V_{appl} (Fig. 2-3).

2. the net charge which resides at the phosphor/insulator interfaces due to the transport of electrons (conduction) during device operation. This charge is defined as the polarization charge, Q_{pol}.

Using the *principle of superposition*, we can treat each component separately and sum up their individual effects to obtain the total characteristics of the device. In this discussion, we neglect the effect of space charge in the phosphor, although, in principle, it could be included as a third component. We also initially ignore leakage charge or any device asymmetry.

Consider the case when the applied voltage is less than the threshold voltage (V_{th}). The effect of the external applied potential in the absence of polarization charge is considered first. If the applied potential, V_{appl}, is positive, the Al electrode becomes positively charged and the ITO electrode becomes negatively charged. The amount of charge stored on either electrode due to the applied potential, Q_{appl}, is related to the total capacitance of the dielectric stack, C_t, by

$$Q_{appl} = C_t \cdot V. \tag{2-5}$$

For example, using the values in Table 2-1 (a) and an applied potential of 100V, gives a charge of 0.72 $\mu C/cm^2$. Moreover the voltage drop across any film can be calculated according to:

$$\Delta V_i = \frac{Q_{appl}}{C_i}. \tag{2-6}$$

Table 2-2. Electric field components due to external voltage, polarization charge, and total, for an applied potential of 100V and a polarization charge of 0.7 $\mu C/cm^2$.

Film	E_{appl} (MV/cm)	E_{pol} (MV/cm)	E_{total} (MV/cm)
ATO	-0.64	0.37	-0.27
ZnS:Mn	-0.99	-0.39	-1.38
SiON	-1.46	0.84	-0.62
Total	(-0.99)	(0)	(-0.99)

where the subscript *i* represents any dielectric in the stack. Figure 2-6 shows the voltage vs. position in the device due to an external applied voltage of 100V in the line marked "External Voltage." In this plot, the parts which correspond to each dielectric layer are also delineated. The electric field, E, due to this external applied voltage is given by,

$$E_i = -\frac{\Delta V_i}{d_i}, \tag{2-7}$$

or the negative slope of the potential vs. position, and is given in the column marked E_{appl} in Table 2-2. The charge stored on the electrodes leads to an electrical displacement in each of the three dielectrics which opposes the electric field due to the applied potential. The external charge, and resulting displacement charges are shown schematically in Figure 2-7 (a). The magnitude of the displacement charge, Q_i^{dis}, is given by:

$$Q_i^{dis} = -\left(Q_{appl} + \varepsilon_o E_{appl,i}\right), \tag{2-8}$$

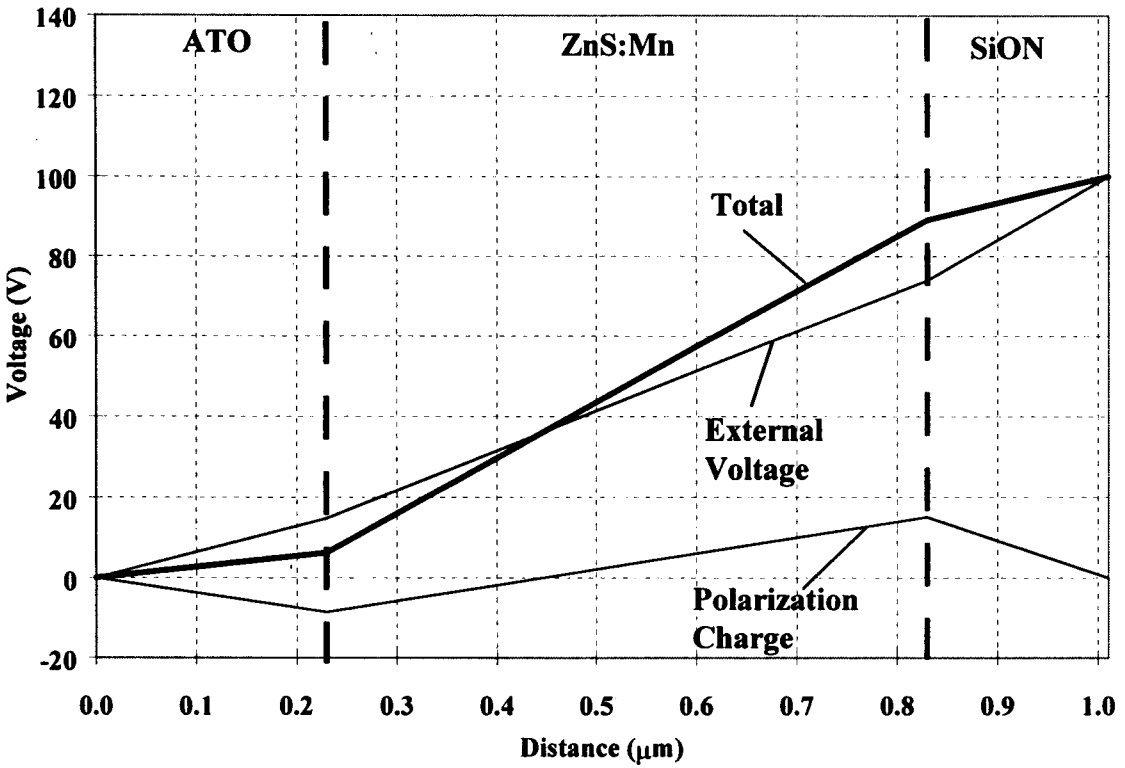

Figure 2-6. Components leading to the potential distributions across an ideal ACTFEL device at an applied potential of 100V and with a polarization charge of 0.7 $\mu C/cm^2$.

(a) Applied Potential, Q_{appl}=0.72μC/cm²

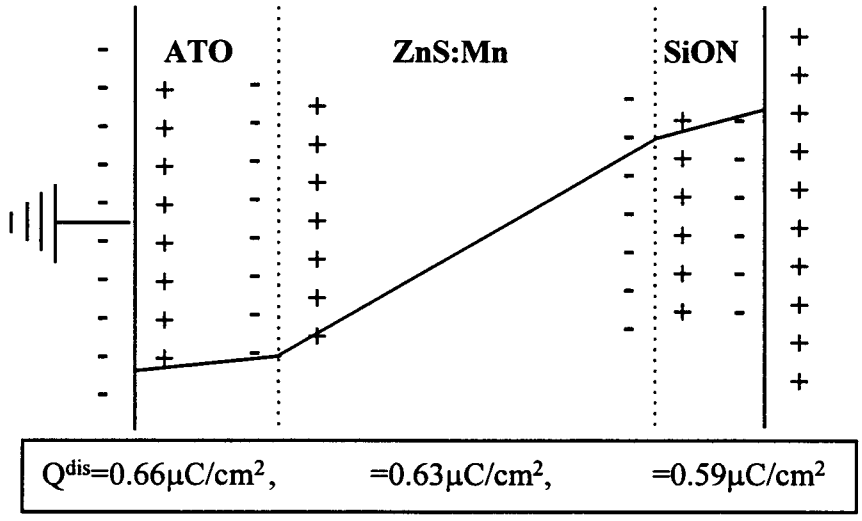

(b) Polarization Charge, Q_{pol}=0.70μC/cm²

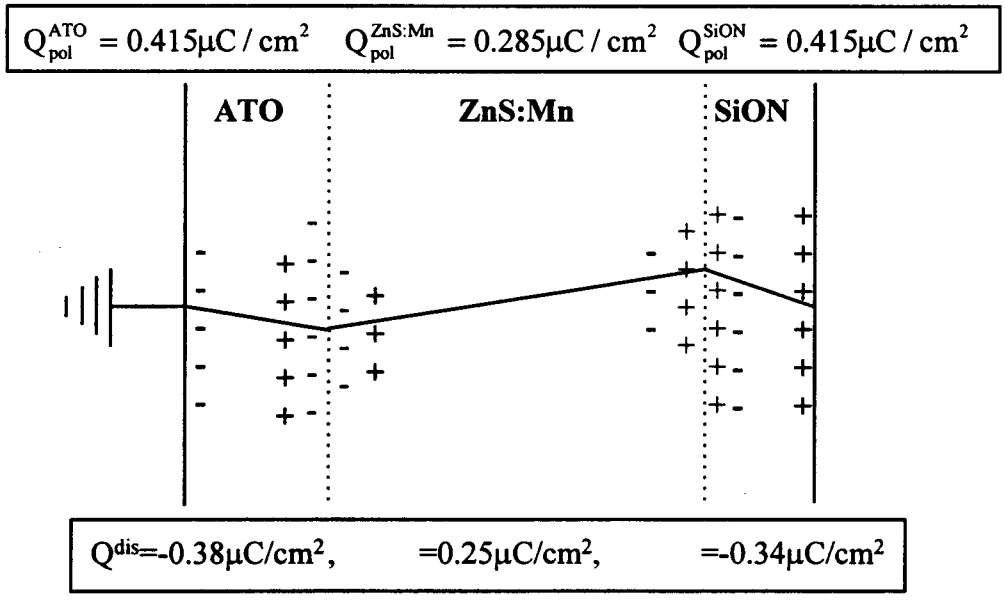

Figure 2-7. Charges and displacement charges in the insulator/phosphor/ insulator stack due to (a) an external applied potential of 100V and (b) polarization charge of 0.7 μC/cm². Parameter values used to come up with the displacement charges are given in Table 2-1.

where ε_0 is the permitivity of free space. Values of the displacement charge are also given in Figure 2-7 (a).

Under steady state operation, the polarization charged stored at the phosphor-insulator interfaces between voltage peaks also contributes to the potential distribution in the device. Before the positive pulse, we have a net negative charge residing at the ATO-phosphor interface and a net positive charge at the phosphor-SiON interface. For the purpose of discussion in this section, we take for a typical value of the polarization charge at steady state, $Q_{pol} = 0.7\ \mu C/cm^2$.

Again this polarization charge leads to electrical displacement in both the insulators and the phosphor. If we consider the contribution of the polarization charge in the absence of an external field (such as is the case between voltage pulses), we know that the sum of the voltage drops across the three dielectric layers must balance:

$$\Delta V_{pol}^{ATO} + \Delta V_{pol}^{ZnS:Mn} + \Delta V_{pol}^{SiON} = 0. \tag{2-9}$$

Rewriting in terms of capacitances gives:

$$\frac{Q_{pol}^{ATO}}{C_{ATO}} + \frac{Q_{pol}^{ZnS:Mn}}{C_{ZnS}} + \frac{Q_{pol}^{SiON}}{C_{SiON}} = 0, \tag{2-10}$$

where Q_{pol}^{i} refers to the fraction of charge in each film, *i*, due to the net charge stored at the phosphor insulator interfaces. Additionally

$$\left|Q_{pol}^{ATO}\right| + \left|Q_{pol}^{ZnS:Mn}\right| = \left|Q_{pol}^{SiON}\right| + \left|Q_{pol}^{ZnS:Mn}\right| = \left|Q_{pol}\right|. \tag{2-11}$$

Thus the solution is reached when the displacement charge is divided sufficiently among the insulators and the phosphor to satisfy the no voltage drop

condition (Eqn. 2-9). The portion of the polarization charge that leads to electrical displacement in the insulators is termed the "external" polarization charge, i.e.,

$$Q_{pol}^{e} = Q_{pol}^{ATO} = Q_{pol}^{SiON}. \tag{2-12}$$

Values are given in Figure 2-7 (b). A plot of the potential which results from the polarization charge is also shown in Figure 2-6 (b), under the line marked "Polarization Charge." Likewise the electric field due to this component (again the negative slope) is reported in Table 2-2.

The potential across the dielectric layers in the device is given by the sum of the two contributions described above. As can be seen from Figures 2-6 and 2-7, the effect of polarization charge is to decrease the potential drop across the insulators and increase the potential drop in the phosphor. Since the electric field is the negative of the slope of potential vs. position, the electric fields in the insulators decrease while the electric field in the phosphor increases. The total electric field is also given in Table 2-2. The external charge can be calculated from the total electric field at either insulator

$$Q^{e} = Q_{tot}^{ATO} = -E_{tot}^{ATO} d_{ATO} C_{ATO} = \Delta V_{tot}^{ATO} C_{ATO} = 0.30\mu C/cm^2 \tag{2-13a}$$

$$= Q_{tot}^{SiON} = -E_{tot}^{SiON} d_{SiON} C_{SiON} = \Delta V_{tot}^{SiON} C_{SiON} = 0.30\mu C/cm^2. \tag{2-13b}$$

The external charge is also given by the sum of the two components discussed above:

$$Q^{e} = Q_{appl} + Q_{pol}^{ATO} = 0.3\mu C/cm^2 \tag{2-14a}$$

$$= Q_{appl} + Q_{pol}^{SiON} = 0.3\mu C/cm^2. \tag{2-14b}$$

While the charge in the phosphor, is given by:

$$Q^{ZnS:Mn} = -E_{tot}^{ZnS:Mn} d_{ZnS:Mn} C_{ZnS:Mn} = \Delta V_{tot}^{ZnS:Mn} C_{ZnS:Mn} = 1.0\mu C / cm^2 \quad (2\text{-}15a)$$

$$= Q_{appl} + Q_{pol}^{ZnS:Mn} = 1.0\mu C / cm^2 . \quad (2\text{-}15b)$$

We now explore how the two components which contribute to the electrical characteristic of the ACTFEL device behave during different parts of the applied voltage pulse. If we consider the potential distribution across the device at any potential lower than threshold voltage (A-B portion of Figure 2-3), the picture is similar to Figure 2-6. The contribution of the external potential will scale in proportion to the applied potential while that from the polarization charge will remain the same as shown in Figure 2-6.

Some important conclusions about electrical characteristics of an ACTFEL device at voltages below the threshold voltage:

- The contribution due to the external field raises proportionately in all three dielectric films.
- The contribution due to the polarization charge remains constant (assuming no leakage charge).
- The value of the phosphor electric field increases with applied voltage.

Now we can consider an applied voltage above the threshold voltage (the B-C portion of Figure 2-3). Eqns. 2-3 to 2-15 are still valid. However, the polarization charge is no longer constant at $0.7\mu C/cm^2$ but changes as electrons transport across the phosphor. If we assume the phosphor field is "clamped", the total electric field across the phosphor layer remains constant at -1.38 MV/cm. Plots of each component and of the voltage for a series of points after phosphor breakdown are shown in Figure 2-8. Specifically, applied voltages of 100, 120, and 160V are shown. We can see that the

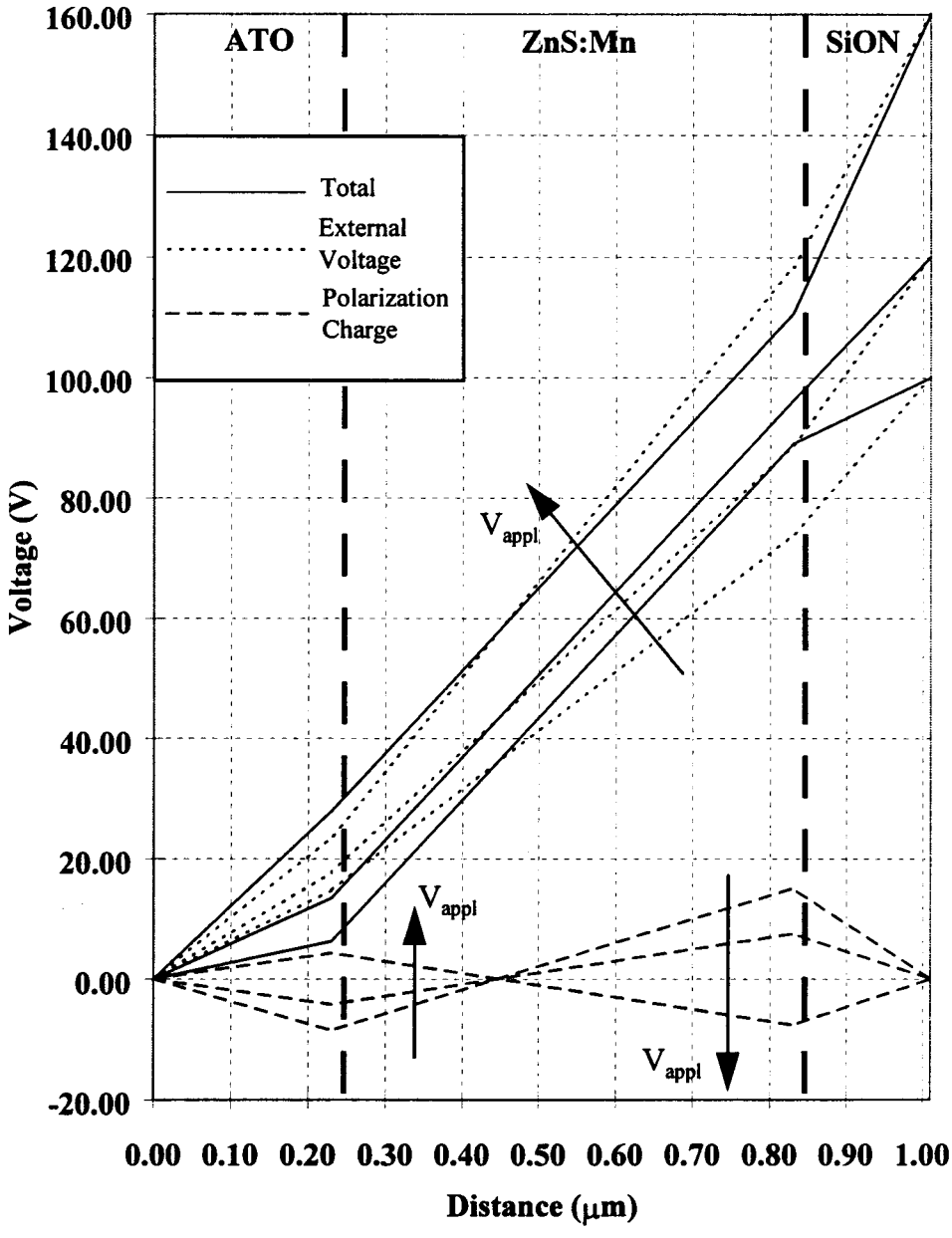

Figure 2-8. Potential distibutions across an ideal ACTFEL device with applied voltage increase from 100 to 160V (arrows indicate increasing V_{appl}).

effect of the external voltage is counteracted by the effect due to the polarization charge. As the phosphor field component from the applied voltage becomes larger in magnitude (more negative), the component to the polarization charge becomes smaller, crosses though zero, and then changes in sign. After the sign change, the net field in the phosphor becomes less than the component from the external voltage. In these plots, we assume electrons transport enough polarization charge across the phosphor to keep the electric field constant, i.e., field clamping. Another alternative would be for the applied voltage field component across the phosphor to rise more rapidly than the polarization component falls. In this case, there would be no field clamping and the total phosphor field would increase with voltage. Both scenarios manifest in real ACTFEL devices.

When the applied voltage reaches V_{max} (in this case at V_{th}+60V=160V), it is held constant for 30μs (C-D portion of Figure 2-3). During this portion of the waveform, electrons still conduct across the phosphor. Potential distributions are shown for points C and D in this portion of the waveform in Figure 2-9. Note, the arrows indicate the evolution of the distribution with time. The accumulated charge at the insulator-phosphor interfaces continues to increase until it matches the polarization charge as before the voltage pulse (but with opposite polarity). The increase in the polarization charge cause the phosphor field to decrease. Understandably, the decrease of the phosphor field during this portion of the waveform is called phosphor field relaxation.

Figure 2-10 shows plots of the potential distribution after the applied voltage start to decrease (D-E portion of Figure 2-3). Since electrons no longer transport across the phosphor, the polarization charge remains constant during this portion of the waveform. The figure shows the slope of potential vs. position in phosphor region changes from positive to negative as the applied voltage decreases, i.e., the phosphor

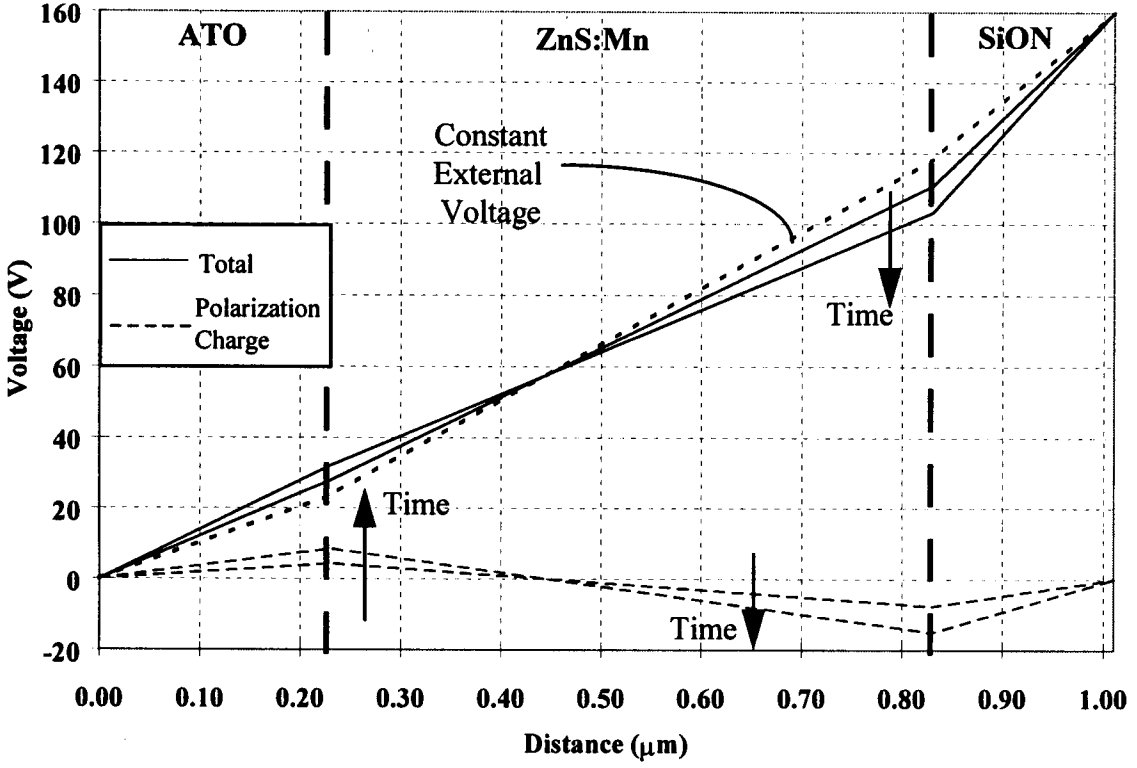

Figure 2-9. Potential distribution across an ideal ACTFEL device with an applied voltage of V_{max} =160V (arrows indicate progressing time, from the rising edge to the falling edge of V_{max}).

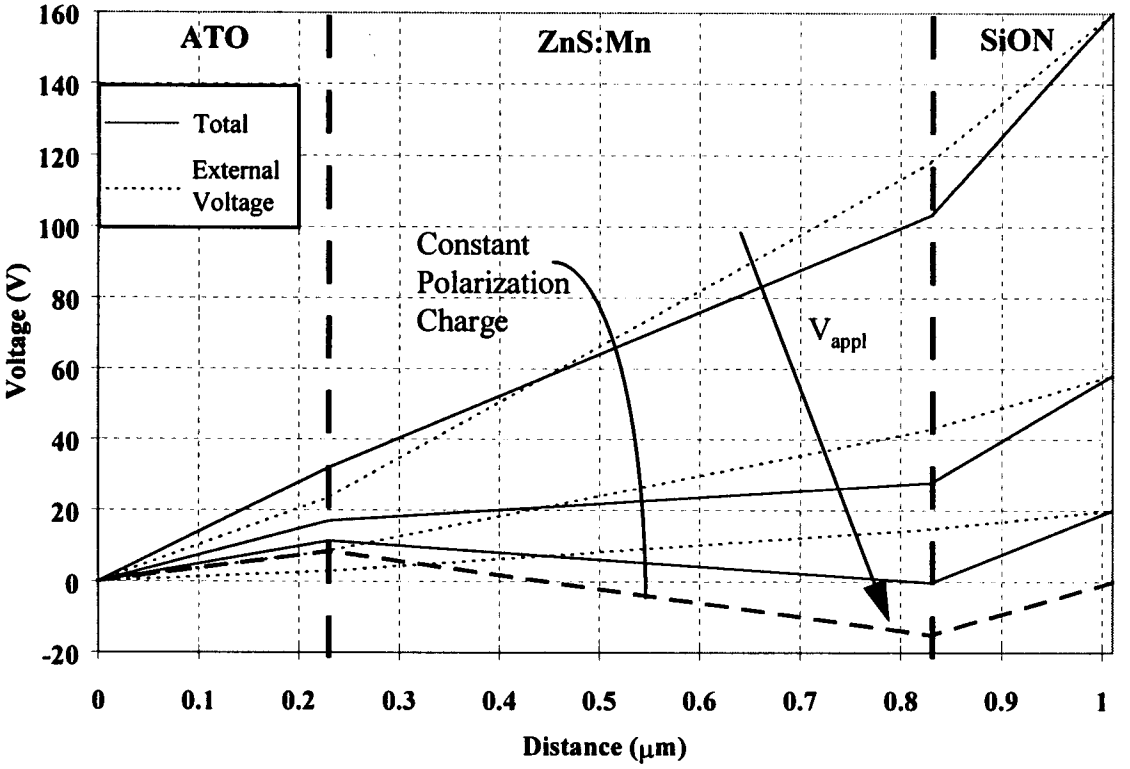

Figure 2-10. Potential distribution across an ideal ACTFEL device with applied voltage decrease from V_{max} to 0V (arrow indicate decreasing V_{appl})

field changes in direction. Again the total distribution is obtained from the sum of applied field and polarization charge components.

This model can be used to construct ideal plots of parameters measured during electrical characterization. Figure 2-11 shows (a) an external charge-voltage (Q-V) curve and (b) an internal charge-phosphor field ($Q\text{-}F_p$) curve. The Q-V curve is obtained by plotting the external charge, Q^e (Eqn. 2-14) versus external applied voltage, V_{appl}. The $Q\text{-}F_p$ is obtained by plotting polarization charge, Q_{pol}, versus electric phosphor field, which can be calculated by setting Eqns. 2-15, equal and solving for $E_{tot}^{ZnS:Mn}$.

$$E_{tot}^{ZnS:Mn} = \frac{Q_{appl} + Q_{pol}^{ZnS:Mn}}{d_{ZnS:Mn} \cdot C_{ZnS:Mn}} = \frac{Q^{ZnS:Mn}}{d_{ZnS:Mn} \cdot C_{ZnS:Mn}}. \qquad (2\text{-}16)$$

In order to present a more realistic plots of Q-V and $Q\text{-}F_p$ curves, a leakage charge of 0.2 $\mu C/cm^2$ is added to the model and plotted in Figure 2-12. In these plots, the points EF and AJ no longer coincide as in Figure 2-11. In order to maintain the polarization charge of 0.7 $\mu C/cm^2$ as in the case where there is no leakage charge, the addition of the leakage charge increases the conduction charge from 1.4 to 1.6 $\mu C/cm^2$. Thus in real device, the existence of leakage charge reduces the internal charge available for polarization of the next polarity of waveform.

The Experimental Q-V and $Q\text{-}F_p$ curves of a typical HTCVD ACTFEL device is presented and discussed in Chapter 3. Note, the slope of the A-B portion of Q-V curves in Figure 2-11 (a) and 2-12 (a) is equal to total capacitance of three dielectric in series, while the slope of the B-C portion of the Q-V curve is equal to the capacitance value of two insulators in series. The sharp change in the slopes is an indication of field clamping. Field clamping is also depicted in Figure 2-11 (b) and 2-12 (b) by the constant phosphor field at the B-C portion of the $Q\text{-}F_p$ curves.

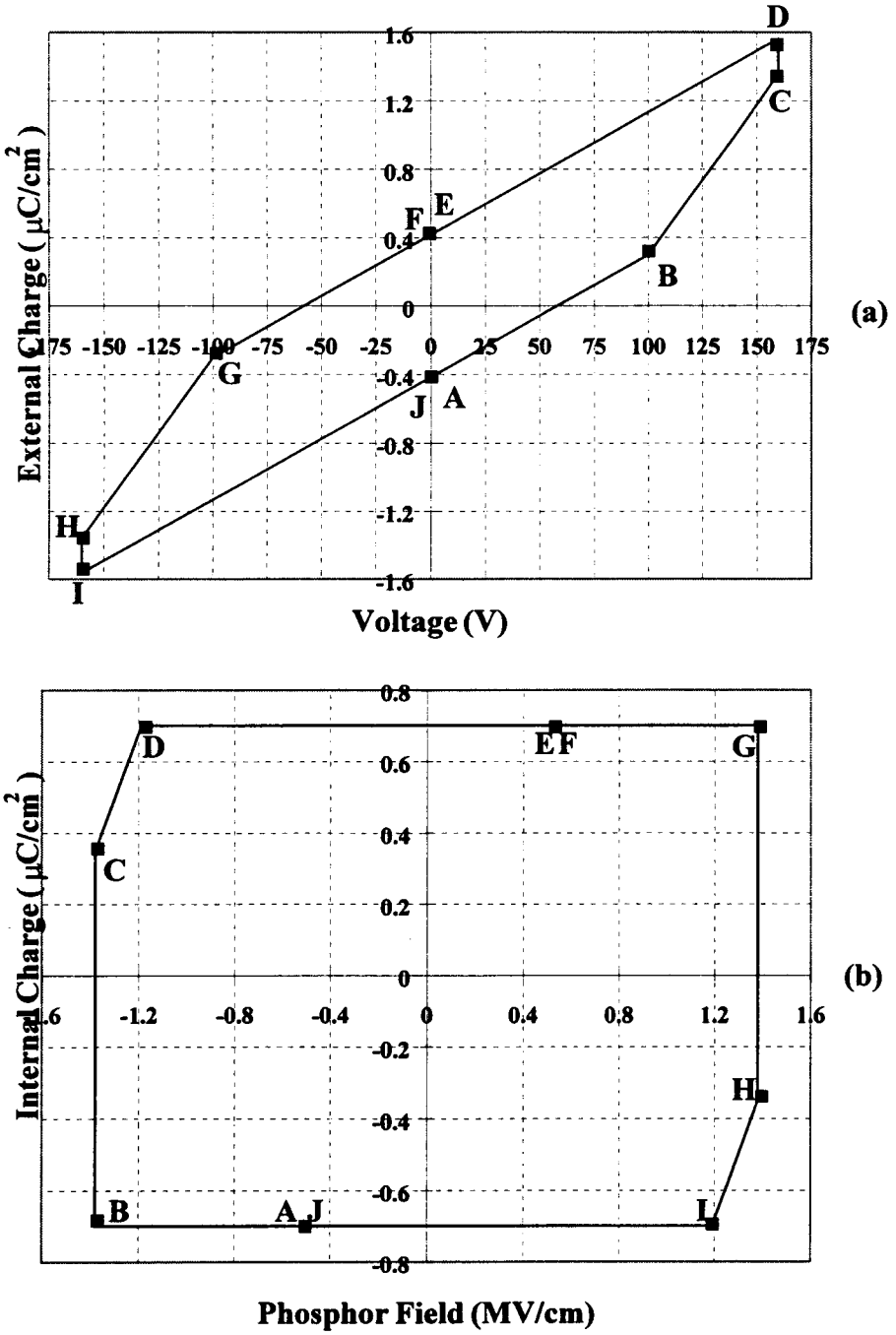

Figure 2-11. (a) Q-V and (b) Q-F_p curves for an ideal ACTFEL device with $V_{max}=V_{th}+60V$ and no leakage charge.

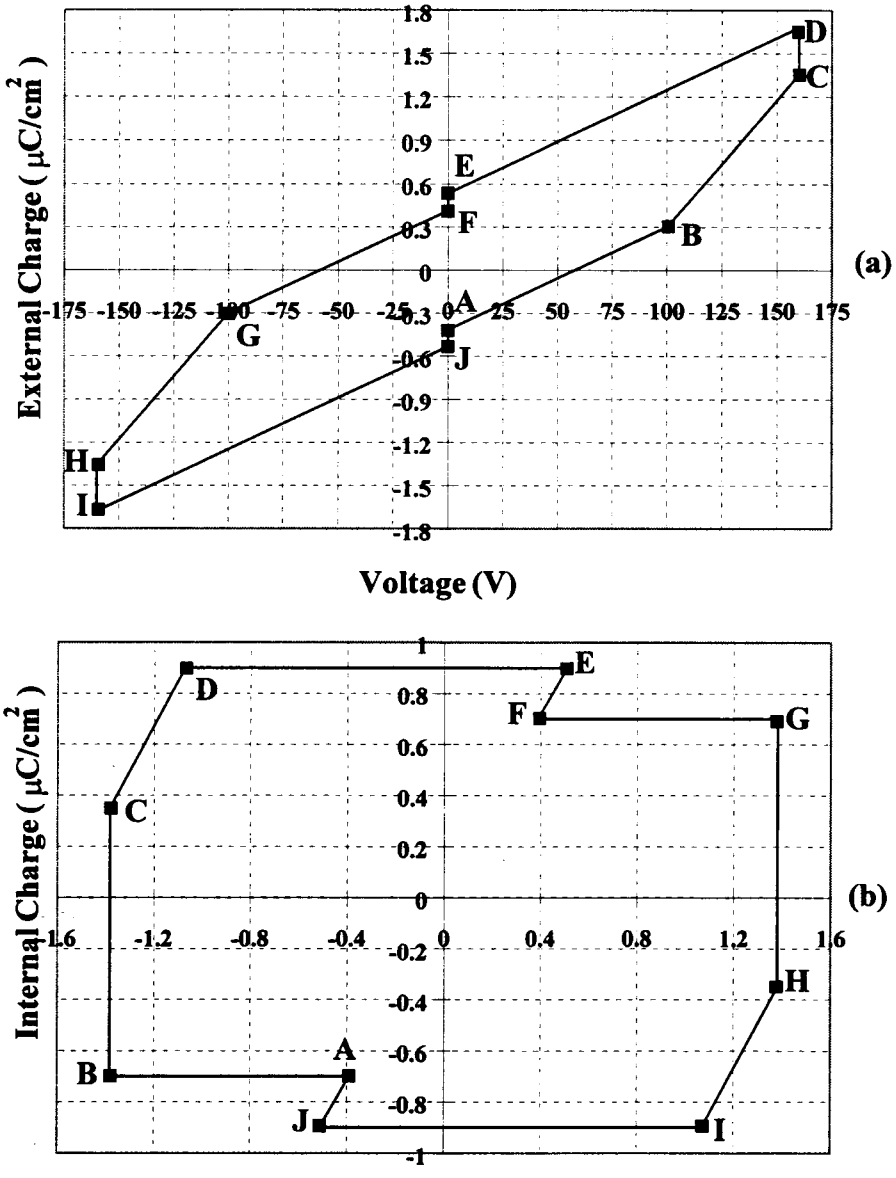

Figure 2-12. (a) Q-V and (b) Q-F_p curves for an ideal ACTFEL device with $V_{max}=V_{th}+60V$ with leakage charge of 0.2 $\mu C/cm^2$.

Chapter 3

EXPERIMENTAL TECHNIQUES

The experimental techniques used in this study can be divided into two major parts: device fabrication and electrical characterization. Device fabrication includes growth of ZnS:Mn by halide transport chemical vapor deposition (HTCVD), growth of silicon oxynitride (SiON) by plasma enhanced chemical vapor deposition (PECVD), and deposition of Al by thermal evaporation. AC-driven thin film electroluminescent (ACTFEL) device characterization includes capacitance-applied voltage (C-V), transfered charge-applied voltage (Q-V), and transfered charge-phosphor field (Q-F_p), and brightness-voltage (B-V) measurements. A detailed description of these methods follows:

3.1 HTCVD ZnS:Mn ACTFEL Device Fabrication

Corning 7059 glass substrates with ATO and ITO thin film layers have been supplied by Planar Systems, Inc. Both ATO and ITO layers are deposited by sputtering. The thicknesses of the ATO and ITO films are around 2300 Å and 3400 Å, respectively.

The ZnS:Mn phosphor layer is deposited by low-pressure HTCVD. A schematic of the HTVCD system is shown on Figure 3-1. A three-zone horizontal resistive furnace provides a base temperature between 470 and 550 ^{o}C. The stainless steel shell acts as a pressure barrier. Inside the shell is a graphite reaction chamber and two source heaters. Source heaters are made of graphite tubing with heating wire wrapped in ceramic tubes placed around the graphite. Nichrome and molybdenum

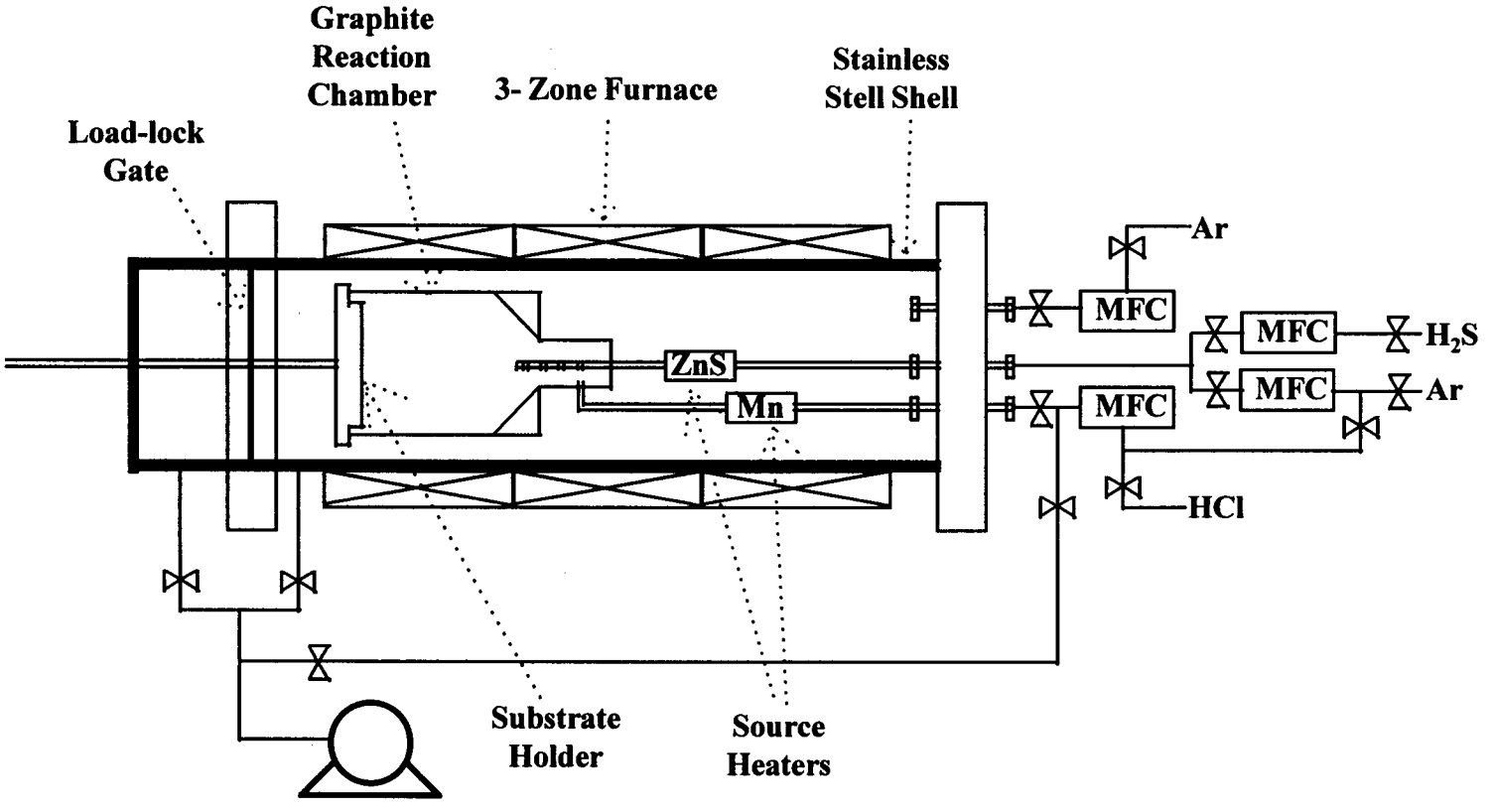

Figure 3-1. Schematic diagram of the halide transport chemical vapor deposition (HTCVD) system.

wires are used as resistive heating wire for the Mn and ZnS source heaters, respectively. Temperature is monitored and controlled separately at the substrate and inside the source heaters. Pressure is maintained below 200 mTorr by a roots blower backed by a mechanical pump. A load lock chamber facilitates easy loading and unloading of samples. A detail of HTCVD design and operation procedures can be found in theses by Miller [1995] and Chen [1998].

High purity ZnS (ESPI, 99.99%) and Mn (ESPI, 99.997%) pellets are used as source materials. For carrier gases, high purity HCl (ESPI, 99.997%), Ar (Air Product, 99.9995%) and H_2S (Air Product, 99.9995%) are used. Grade 5 N_2 gas is used for cleaning the glass substrate and purging the system.

The ranges of process parameters are given in Table 3-1. Substrate temperature, ZnS and Mn source temperatures, Ar, H_2S and HCl gas flow rates, and deposition time are controllable process parameters. The quality and characteristics of deposited phosphor film depend on these process parameters. For optimization of process condition for ZnS:Mn phosphor layer fabrication, a design of experiments (DOE) is employed. The details of the DOE are presented in Section 3.7.

After ZnS:Mn phosphor deposition, 2000 Å of SiON is deposited. Plasma enhanced chemical vapor deposition (PECVD) with a pressure of 700 mTorr, a

Table 3-1. HTCVD process parameters and values.

Substrate temperature	470 - 550 °C
ZnS source temperature	900 - 980 °C
Mn source temperature	725 - 775 °C
Ar flow rate	40 sccm
H_2S flow rate	0 - 0.4 sccm
HCl flow rate	0.7 - 3 sccm
Deposition time	3 hours

substrate temperature of 300 °C and RF power of 60 Watt is used for all samples. The electrode configuration is parallel plate. SiH_4, N_2O and N_2 gases flow at rates of 85, 2.5 and 375 sccm, respectively. The films obtained have an index of refraction of 1.6 (corresponding to dielectric constant of 5.0). Lastly, aluminum dots are deposited on top of SiON insulating layer by thermal evaporation. Each aluminum dot has an area of 0.085 cm^2 and thickness of 2000 Å.

3.2 HTCVD ZnS:Mn ACTFEL Device Characterizations

The physical apparati of electrical and optical characterization employed in this study have been designed and constructed by members of Electrical and Computer Engineering Department at Oregon State University [Douglas, 1993; Abu-Dayah, 1993; Shih, 1996]. Electrical characterization includes charge-voltage (Q-V), capacitance-voltage (C-V) and internal charge-phosphor field (Q-F_p) measurements. Brightness-voltage (B-V) measurements have also been used. All these characterization techniques employ a Sawyer-Tower configuration which is shown in Figure 3-2. The circuit consists of an arbitrary waveform generator (Wavetek model 395), a home-made high voltage amplifier (max.: 300 volts), a 500 Ω current-limiting resistor (Series Resistor), the ACTFEL device under test, and a 103.9 nF capacitor, as a sensing element. A digital oscilloscope (Tektronix TDS 420) is used to sample and digitize the applied voltage. The collected data (V_2 and V_3) are then downloaded into a personal computer (PC) for further manipulation.

The electrical characterization techniques are used to obtain both internal, and external electrical quantities of the device as defined in Section 2-7. The internal quantities refer to quantities that relate to the properties of phosphor layer only, while the external quantities refer to the properties of the ACTFEL device as a whole. The Q-V measurement is used to obtain both internal quantities, such as conduction charge

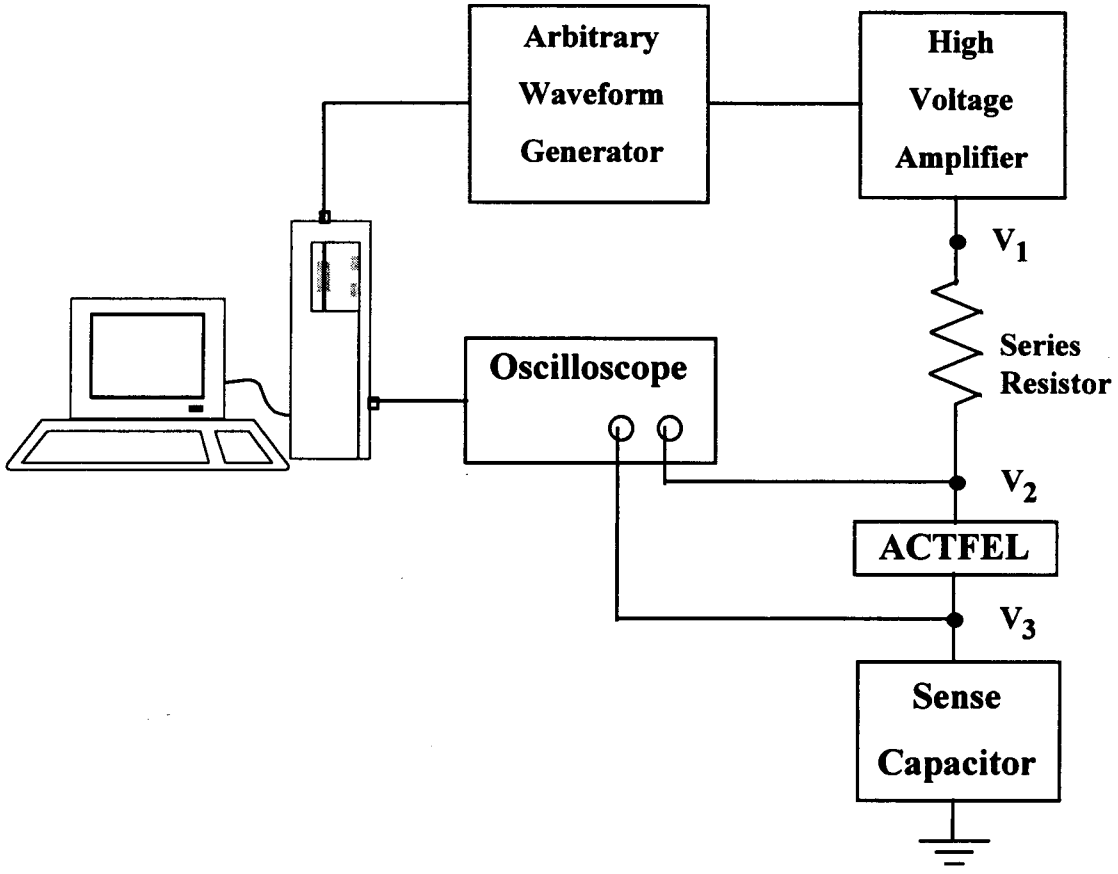

Figure 3-2. Sawyer-Tower configuration for electrical characterization.

(Q_{cond}) and relaxation charge (Q_{relax}), and external quantities such as polarization charge (Q_{pol}), leakage charge (Q_{leak}), turn-on voltage, insulator capacitance, and phosphor capacitance. The C-V measurement only measures external quantities such as turn-on voltage, total capacitance, insulator capacitance, phosphor capacitance and the interface state density in the pre-clamping regime. The Q-F_p technique only measures internal quantities such as Q_{cond}, Q_{pol}, Q_{relax}, and Q_{leak}, and the steady state field (F_{ss}) inside the phosphor. More about both internal and external quantities will be said in later sections.

3.3 Capacitance-Voltage (C-V) Measurement

The C-V measurement is performed by monitoring the voltages on both sides of the ACTFEL device as the applied external voltage varies. The capacitance of the device is determined by the following equation,

$$C(t) = \frac{dQ(t)}{dV(t)} = \frac{d[C_{sense} \cdot V_3(t)]}{d[V_2(t) - V_3(t)]}, \qquad (3\text{-}1)$$

where C_{sense} is the sense capacitor. $V_2(t)$-$V_3(t)$ is the voltage drop across the ACTFEL device.

A C-V plot obtained from a representative HTCVD ZnS:Mn ACTFEL device is shown in Figure 3-3. The curve for increasing voltage is shown with arrow pointing to the right, while the left pointing arrow shows the curve for the falling edge of the applied waveform. Figure 3-3 shows when the applied voltage increases from 0 to 60 V, the calculated capacitance is equal to the total capacitance (C_t). C_t is equal to the phosphor capacitance (C_p) and both insulator capacitances (C_i) in series, as shown in Figure 2-5 (ACTFEL device equivalent circuit). This device has a total capacitance of 9.2 nF/cm^2. V_{to1} (~80 V) is the minimum external applied voltage required for

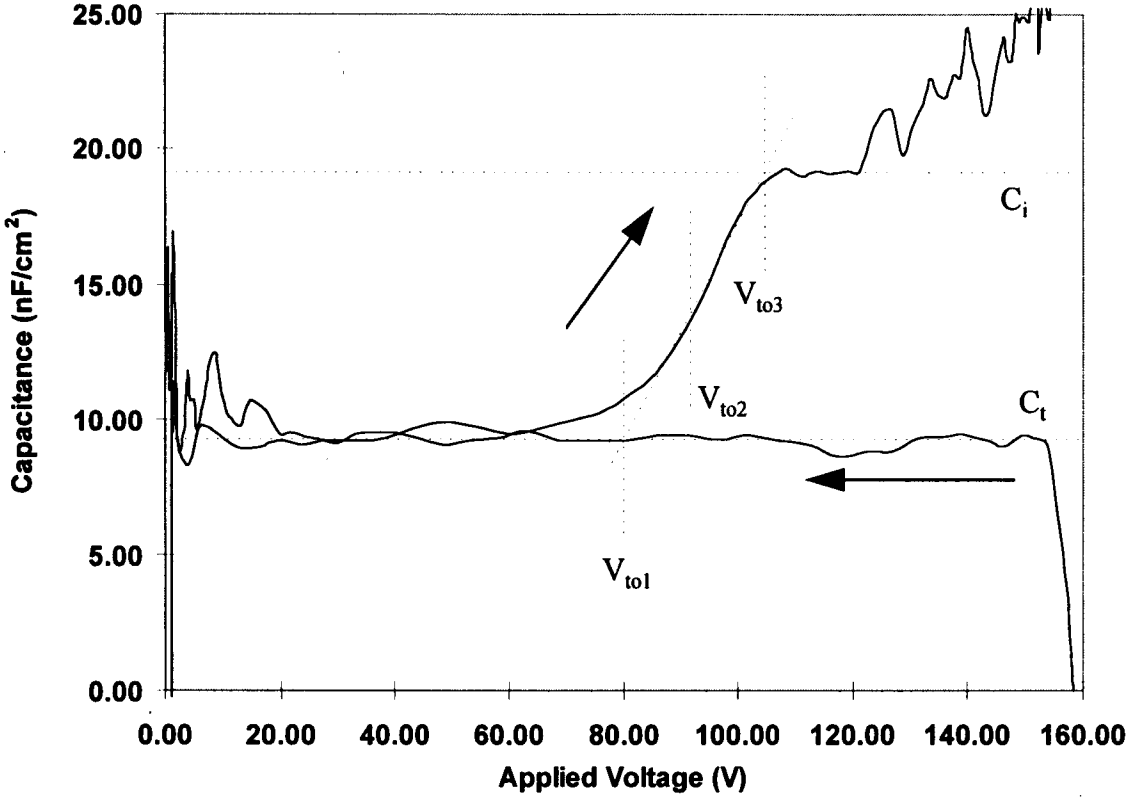

Figure 3-3. C-V curve for HTCVD ZnS:Mn ACTFEL device.

electrons to tunnel out of energy states at the phosphor-insulator interface into the phosphor conduction band. The magnitude of V_{to1} depends on the magnitude of the polarization charge (Q_{pol}). V_{to2} (~90 V) corresponds to the threshold voltage obtained from the Q-V curve, and is independent of any polarization charge stored at the interface. V_{to3} (~105 V) corresponds to threshold voltage at the initiation of field clamping. At this external voltage, the interface trap density is of sufficient magnitude that the phosphor field remains constant. In Section 2.7, we assumed $V_{to1}=V_{to2}=V_{to3}$, but in real devices, this is usually not the case. Above the threshold voltage, the phosphor capacitance breaks down, therefore the calculated capacitance increases to the value of the total insulator capacitance (C_i). This device has an insulator capacitance of 19.0 nF/cm^2. The physical capacitance value is 17.6 nF/cm^2. This difference in total insulator capacitance can be explained by space charge generation in the phosphor layer. Space charge generation tends to yield a calculated total insulator capacitance greater than its physical value. Space charge also causes an overshoot in C-V curve. According to a single sheet charge model developed by Keir *et al.* [1995], the magnitude of overshoot depends on the location of the space charge layer, with the maximum overshoot occurring when the space charge layer exists near the cathodic interface.

The slope of C-V curve is related to the density of interface traps in the sub-field-clamping regime [Davidson *et al.*, 1992] according to the following equation,

$$Q_{ss} = \frac{C_i^{\,2}}{2q}\frac{C_t}{C_p}\left[\frac{\Delta C}{\Delta V}\right]^{-1}, \tag{3-2}$$

where: Q_{ss} = the interface state density (# of states/cm^2),

ΔC = C_i-C_t (nF/cm^2), and

ΔV = V_{to3}-V_{to1} (V).

This device has an interface state density of 1.5×10^{12} # of states/cm^2. A large interface state density is required for electron sourcing and proper ACTFEL device operation. A large interface state density is also required for field clamping.

According to Davidson [1991] the unrealistically large capacitance rise near the maximum voltage (V_{max}) is a feature of the C-V measurement rather than evidence of leakage in or charge injection into the insulating layers.

3.4 External Charge-Voltage (Q-V) Measurement

A Q-V curve is generated by plotting the externally measured charge versus the applied voltage across the ACTFEL device as discussed in Section 2-7. The external charge, Q^e, is calculated by:

$$Q^e(t) = C_{sense} \cdot V_2(t) . \tag{3-3}$$

A Q-V curve for the same ACTFEL device used in the C-V measurement is shown in Figure 3-4. Notice the figure is similar to the ideal behavior presented in Figure 2-12 (a). Again the labels A through J correspond to points of the applied voltage waveform shown in Figure 2-3. Point A corresponds to the onset of a positive voltage pulse applied to the Al electrode. Non-zero values of Q at point A are due to the polarization charge residing at phosphor-insulator interface that was left behind by the previous negative pulse. The AB and BC portion of the Q-V curve arise from the rising portion of the external voltage. Point B is where the ACTFEL device start to turn-on. During CD portions of the waveform, the applied voltage is constant at its maximum amplitude (V_{max}) and the phosphor field relaxes. DE corresponds to the falling portion of the waveform. EF corresponds to the portion of waveform where external bias is zero. The reminder of Q-V curve from point F to point A is similar to

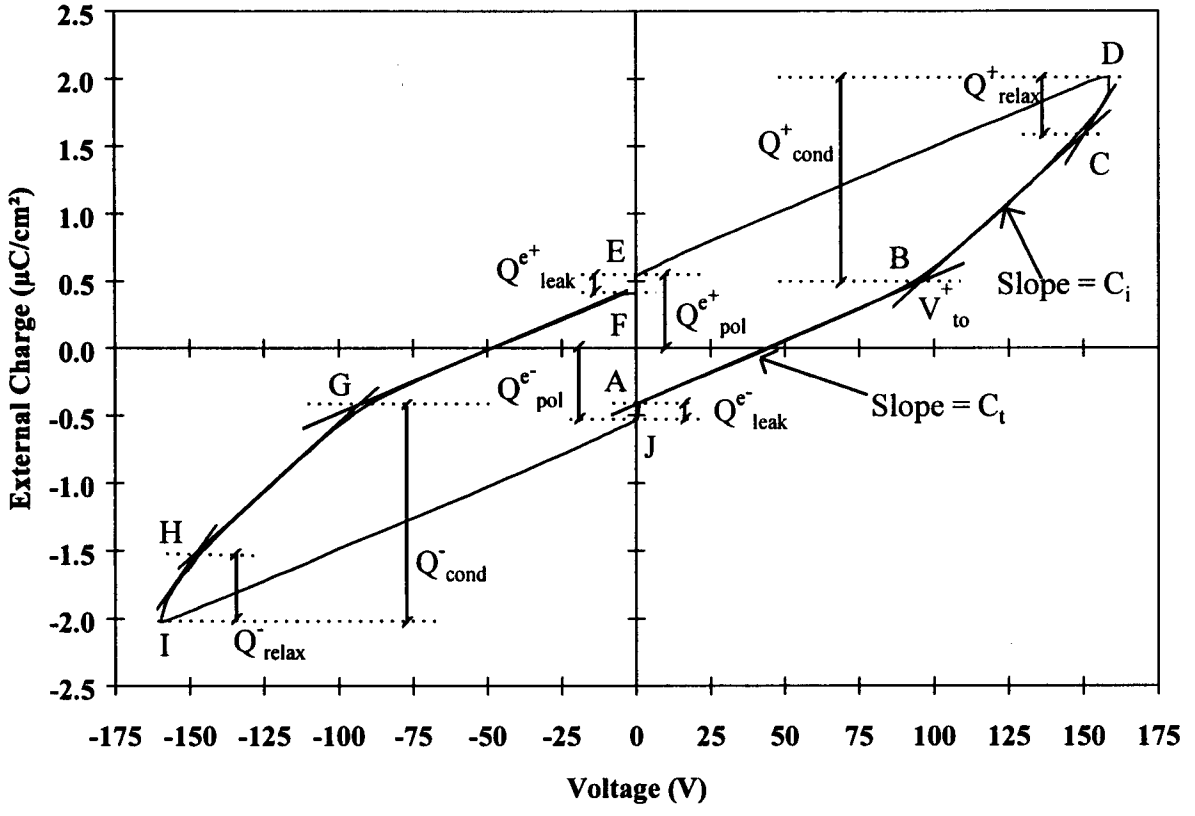

Figure 3-4. Q-V curve for HTCVD ZnS:Mn ACTFEL device.

the point A to point F portion of the curve just described above, except that the external applied voltage pulse is of negative polarity.

The plot shows two different slopes that are equal to the value of total capacitance and insulator capacitance of the ACTFEL device. The dynamic capacitance is defined as

$$C = \frac{dQ}{dV}. \tag{3-4}$$

The constant slope for voltages less than turn-on voltage (V^{+}_{to}), in the region of AB, is equal to the total capacitance (C_t). The slope of region labeled FG is also equal to the total capacitance (C_t) for the negative polarity of the applied voltage. At voltages higher than the turn-on voltage, in the region of BC and GH, conduction current begins to flow through the phosphor layer as the layer breaks down. This break down causes the total capacitance to reduce to the capacitance of both top and bottom insulator layers in series. Values of C_t and C_i from Figure 3-4 are 9.2 and 20.2 nF/cm^2, respectively. The values of C_t and C_i obtained from Q-V curve are used to construct Q-F_p curves. A more detailed discussion of the Q-F_p curve is presented in the next section.

Superscripts '+' and '-' are used to identify the polarity of the applied voltage pulse. A positive voltage pulse is defined as when the Al electrode bias is positive while a negative voltage pulse is defined as when the Al electrode bias is negative. The superscript "e" is used to denote charge that is perceived externally, such as Q_{pol} and Q_{leak}. Charge without such superscript indicates the charge to be an internal charge, such as Q_{cond} and Q_{relax}. The actual internal polarization and leakage charges can be related to their external charges by,

$$Q_{pol} = \frac{C_i + C_p}{C_i} Q^e_{pol}, \tag{3-5}$$

$$Q_{leak} = \frac{C_i + C_p}{C_i} Q^e_{leak} \tag{3-6}$$

as shown in Section 2.7.

3.5 Internal Charge-Phosphor Field (Q-F_p) Measurement

The Q-F_p technique provides direct internal behavior information of ACTFEL device [Abu-Dayah *et al.*, 1993]. The internal charge and the phosphor field are experimentally determined using,

$$Q(t) = \frac{C_i + C_p}{C_i} C_{sense} \cdot V_3(t) - C_p \cdot [V_2(t) - V_3(t)], \tag{3-7}$$

$$F_p = \frac{1}{d_p}\left[\frac{C_{sense} \cdot V_3(t)}{C_i} - (V_2(t) - V_3(t))\right], \tag{3-8}$$

where d_p is thickness of phosphor layer. Both Equations 3-7 and 3-8 are derived from the paper of Bringuier [1992]. The accuracy of the Q-F_p curve relies on the accuracy of values for phosphor capacitance, C_p, insulator capacitance, C_i, and phosphor thickness, d_p. In this study, the values of C_p and C_i are obtained from the Q-V curves such as in Figure 3-4. These values are different from the physical values because of the large amount of dynamic space charge that exists in HTCVD ZnS:Mn ACTFEL devices. Inaccuracy in estimating phosphor thickness will effect the accuracy of F_{ss}, phosphor

steady state field. In this study, the phosphor thickness is generally set at 6000 Å on the previous HTCVD ZnS:Mn study by Chen [1998].

A Q-F_p curve for the same HTCVD ACTFEL device used for both C-V and Q-V measurements, is shown in Figure 3-5. The labels A through J correspond to the points in Figures 2-4, 2-11 (b), and 3-4. Explanations about those points are the same as given in the previous section. Non-zero values of Q-F_p at point A result from the polarization charge residing at phosphor-insulator interface left behind by the previous negative pulse. As discussed in detail in Section 2.7, the phosphor field is constant during much of the BC portion of the waveform and is equal to F_{ss}. The polarity of the phosphor field reverses from positive to negative during ED portion of the waveform. The dotted lines represent the ideal curve derived in Section 2.7. The internal charges obtained from the Q-F_p curve, Q_{cond}, Q_{pol}, Q_{leak} and Q_{relax} have been defined in Section 2.7.

3.6 Brightness-Voltage and Brightness Transient Measurement

Figure 3-6 shows brightness versus applied voltage (B-V) characteristic for a typical HTCVD ZnS:Mn ACTFEL device. Above the threshold voltage, the brightness first increases steeply and then saturates. A B-V [or L-V (Luminance-Voltage)] curve is obtained by plotting the brightness of ACTFEL device under test versus the applied voltage. The device's brightness is measured by using a photometer (Photo Research 650 SpectraScan). The applied voltage waveform used for the B-V measurement is the same as the one used in electrical characterization: bipolar pulses of trapezoidal shape with 5 μs rise and fall time and a pulse width of 30 μs. The frequency of the waveform is 1 kHz.

The brightness transient plots the time evolution of device brightness when a single pulse (from zero to V_{max} and back to zero) of external voltage is applied to the

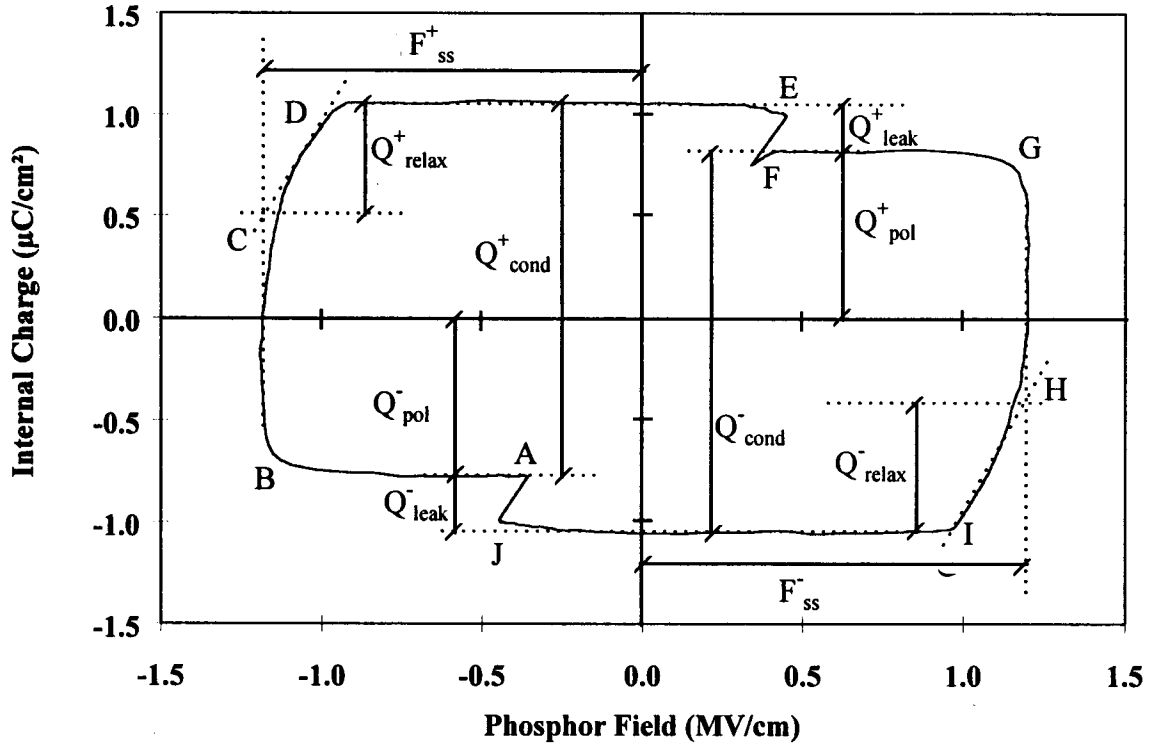

Figure 3-5. Q-F_p curve for HTCVD ZnS:Mn ACTFEL device.

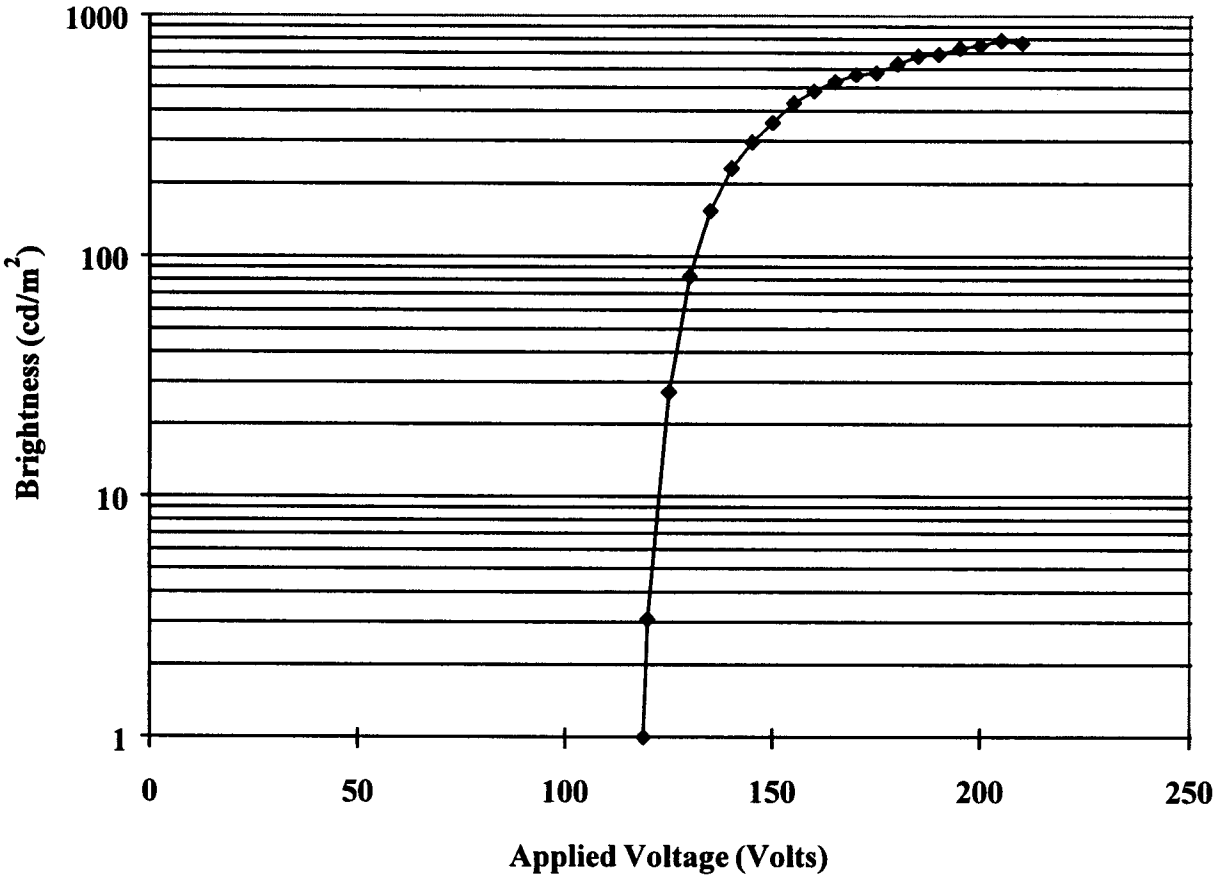

Figure 3-6. B-V curve for HTCVD ZnS:Mn ACTFEL device.

device. The brightness is measured by a photodiode for adequate response. The decay time of light emission can be calculated from a brightness vs. time plot. The decay time is the time required for the light intensity to reduce to 1/e of its maximum value, assuming an exponential decay.

3.7 Design of Experiment for ZnS:Mn Fabrication

There are seven process parameters that can affect the quality and characteristics of deposited phosphor film: substrate temperature, ZnS source temperature, Mn source temperature, Ar carrier gas flow rate, H_2S carrier gas flow rate, HCl carrier gas flow rate, and total deposition time. Out of the seven process parameters, two parameters are set at constant values. The Ar carrier gas flow rate is set at 40 sccm and the deposition time at 3 hours. Each of the remaining parameters, or factors, then can be varied.

Since there are five factors with a maximum level of 4, a modified L16 orthogonal array with a total of 16 runs, 5 factors at 2-4 levels each, is used. The original array is shown in Table 3-2 [Fowlkes, 1995]. Because there is only one factor (HCl carrier gas flow rate) at 4 levels, the rest of the columns in the array are downgraded with a dummy level. The resulting array after downgrading is still orthogonal even though it is no longer exactly balanced. For substrate temperature and ZnS source temperature which have 3 levels each, a dummy level is set for the fourth level. The dummy levels are 550 and 900 ^{o}C for substrate temperature and ZnS source temperature, respectively. Since there are only two levels for Mn source temperature and H_2S flow rate, level 3 and 4 of each factor are set to equal to level 1 and 2, respectively. Table 3-3 shows the different levels and their values for each process factor. Table 3-4 shows the complete design of experiment array for the HTCVD ZnS:Mn phosphor layer fabrication.

Table 3-2. Modified L16 (Five Factors at Four Levels) Array.

Run	1	2	3	4	5
1	1	1	1	1	1
2	1	2	2	2	2
3	1	3	3	3	3
4	1	4	4	4	4
5	2	1	2	3	4
6	2	2	1	4	3
7	2	3	4	1	2
8	2	4	3	2	1
9	3	1	3	4	2
10	3	2	4	3	1
11	3	3	1	2	4
12	3	4	2	1	3
13	4	1	4	2	3
14	4	2	3	1	4
15	4	3	2	4	1
16	4	4	1	3	2

Table 3-3. Design of Experiment Process Factors and Level of Each Factors.

Factors	Levels	Values
Substrate temperature	1	470 °C
	2	500 °C
	3 and 4	550 °C
ZnS source temperature	1 and 4	900 °C
	2	940 °C
	3	980 °C
Mn source temperature	1 and 3	725 °C
	2 and 4	775 °C
H_2S flow rate	1 and 3	0 sccm
	2 and 4	0.4 sccm
HCl flow rate	1	0.7 sccm
	2	1 sccm
	3	2 sccm
	4	3 sccm

Table 3-4. A Complete Design of Experiment Array.

Run	HCl Flow rate	H_2S Flow rate	Mn Source Temperature	ZnS Source Temperature	Substrate Temperature
1	0.7	0.4	725	900	470
2	0.7	0	775	940	500
3	0.7	0.4	725	980	550
4	0.7	0	775	900	550
5	1	0.4	775	980	550
6	1	0	725	900	550
7	1	0.4	775	900	500
8	1	0	725	940	470
9	2	0.4	725	900	500
10	2	0	775	980	470
11	2	0.4	725	940	550
12	2	0	775	900	550
13	3	0.4	775	940	550
14	3	0	725	900	550
15	3	0.4	775	900	470
16	3	0	725	980	500

Chapter 4

RESULTS AND DISCUSSION

In this chapter, the results of the process optimization of HTCVD ZnS:Mn thin film fabrication and electrical characterization of HTCVD ZnS:Mn ACTFEL device are discussed. Process optimization is done through statistical analysis of the brightness-voltage response and through electrical characterization of the ACTFEL device.

4.1 Statistical Analysis of The Brightness-Voltage Response

Figure 4-1 shows box-and-whisker plots for brightness at 60 V above the threshold voltage versus the following reactor parameters: (a) Mn source temperature, (b) ZnS source temperature, (c) substrate temperature, (d) HCl gas flow rate, and (e) H_2S gas flow rate. Inspection suggests there is a maximum in brightness at 2 sccm HCl flow rate and, perhaps, at 550 °C substrate temperature and 0 H_2S flow rate. The other parameters do not appear to have a significant effect. Additionally, the lengths of upper and lower whiskers are not the same in Figures 4-1 (a), (c), and (e) suggesting the data is skewed. The spread (which is related to the box size) is not equal between levels, as shown in all five box plots. The level 0 of H_2S flow rate, for example, has a spread of 220 cd/m^2 while the level 0.4 sccm only has a spread of 92 cd/m^2. Logarithm and natural logarithm transformations of the data do not help to eliminate the skewness and the unequal spread. It is possible the small sample size, i.e., not enough replication of runs, and large process variance causes the skewness and the irregular spread size.

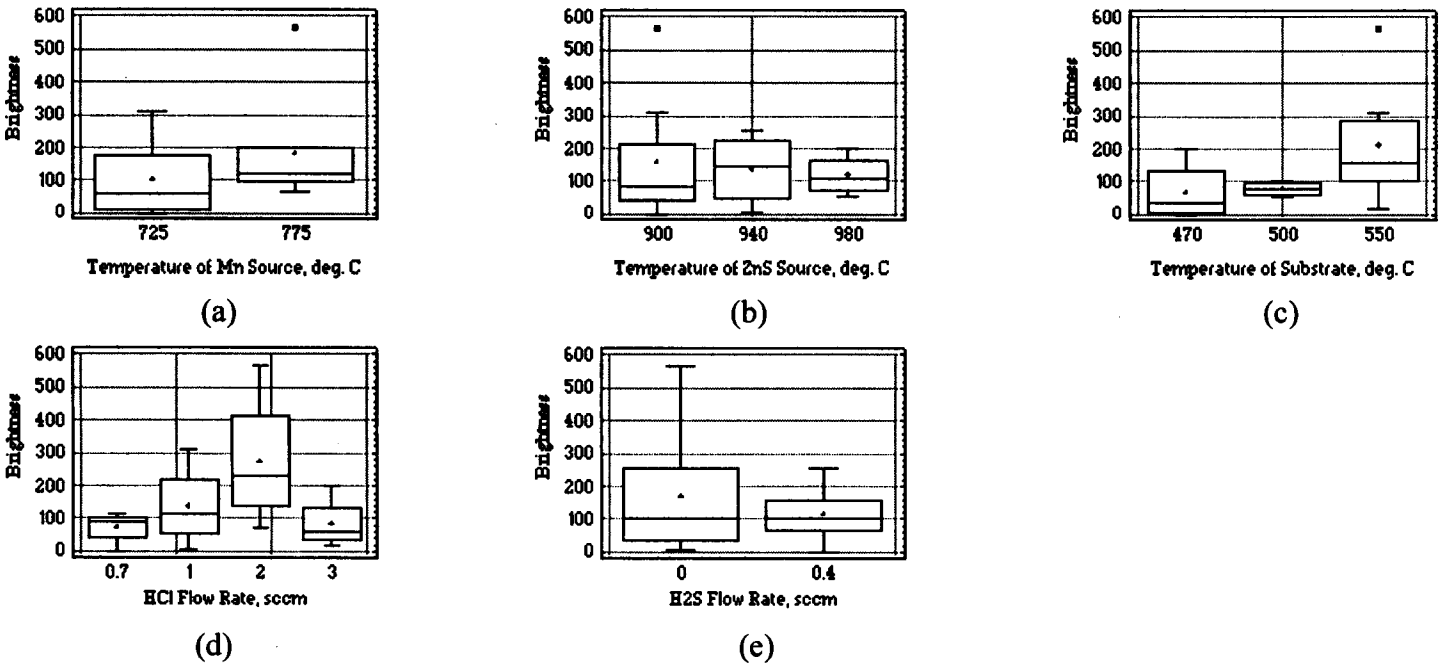

Figure 4-1. Box-and-whisker plots of brightness of ACTFEL device at 60V above the threshold voltage for different process parameters.

Table 4-1. Analysis of Variance for Brightness - Type III Sums of Squares.

Source	Sum of Squares	Df	Mean Square	F-Ratio	P-Value
MAIN EFFECTS					
A: H_2S flow rate	12542.9	1	12542.9	0.84	0.3947
B: HCl flow rate	100107.0	3	33368.9	2.23	0.1847
C: Mn Temp.	26442.3	1	26442.3	1.77	0.2316
D: Substrate Temp.	74728.5	2	37364.3	2.50	0.1621
E: ZnS Temp.	3846.2	2	1923.1	0.13	0.8815
RESIDUAL	89581.7	6	14930.3		
TOTAL (corrected)	307248.0	15			

All F-Ratios are based on the residual mean square error.

Table 4-1 shows an analysis of variance (ANOVA) for brightness. The sum of squares, the degrees of freedom (Df), the Mean Square, the F-ratio and the P-value are obtained in the standard manner [Fowlkes, 1995]. There is no parameter that has a P-values less than 0.05, indicating that, at the 95% confidence level, none of the parameters have a statistically significant effect on the brightness. One explanation for these large P-values is that there is very strong interaction between parameters in this system.

The F-Ratios have values between 0.13 and 2.50. As a rule of thumb, the following rankings can be used [Fowlkes, 1995]:

- F-ratio < 1 : the control factor is insignificant and indistinguishable from the experimental error.
- F-ratio ≈ 2 : the control factor has only a moderate effect compared to experimental error.
- F-ratio > 4 : the control factor is strong compared to experimental error and is clearly significant.

Based on these rules of thumb, the ZnS source temperature and the H_2S gas flow rate, which have F-ratios of 0.13 and 0.84, respectively, are insignificant and indistinguishable from the experimental error. The rest of control factors have F-ratios between 1.77 and 2.50 which means they have a moderate effect compared to experimental error. This conclusion is different than that made by inspection. Also based on the F-ratios, the substrate temperature and the HCl gas flow rate have a relatively stronger effect than to the Mn source temperature.

A three-dimensional plot of the significant process parameters resulting from ANOVA is shown in Figure 4-2. The brightness is plotted against the substrate temperature and the HCl gas flow rate. Data for low Mn source temperature (725 °C) and high Mn source temperature (775 °C) are shown by filled and open squares, respectively. This figure shows that the highest brightness is achieved when the phosphor layer is deposited at substrate temperature of 550 °C.

The determination of the optimum HCl gas flow rate and Mn source temperature are not as clear. Figure 4-3 shows a plot of brightness versus HCl gas flow rate for a substrate temperature of 550 °C. The runs that have Mn source temperature of 725 °C are marked as filled rectangular. At a glance, one would pick 2 sccm for HCl gas flow rate as the optimum level, but it is possible that the highest brightness shown on the plot is due to experimental variation. This particular process condition is shown on Figure 4-1 (a) as an outlier. Figure 4-3 shows two dashed lines that connects points which have the same Mn source temperature but different HCl gas flow rates. These two lines are crisscross. These crisscrossing lines can be interpreted in two ways. It may mean the Mn source temperature has a strong interaction with HCl gas flow rate, especially for the gas flow rate between 1 and 2 sccm. Alternatively, the Mn source temperature has no effect at all to the HTCVD ZnS:Mn deposition process, but rather are just a result of random process variation.

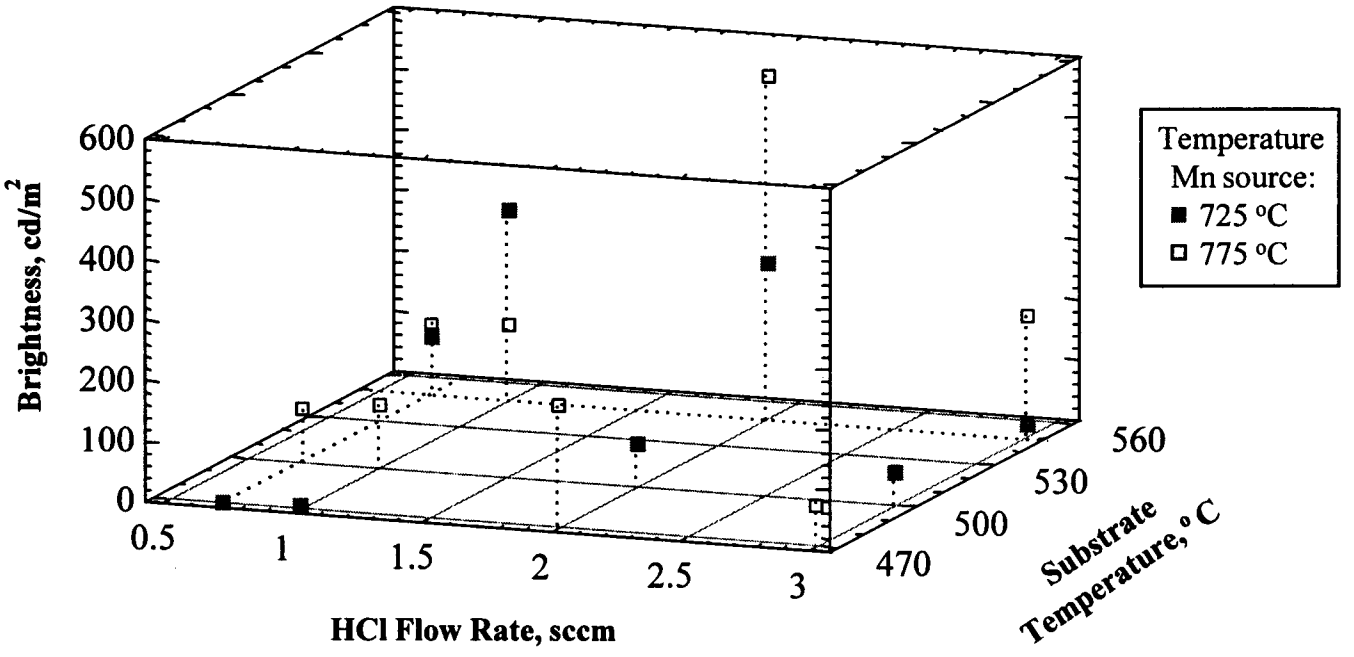

Figure 4-2. 3-D plot of brightness of ACTFEL device versus HCl flow rate and substrate temperature with temperature of Mn source is marked.

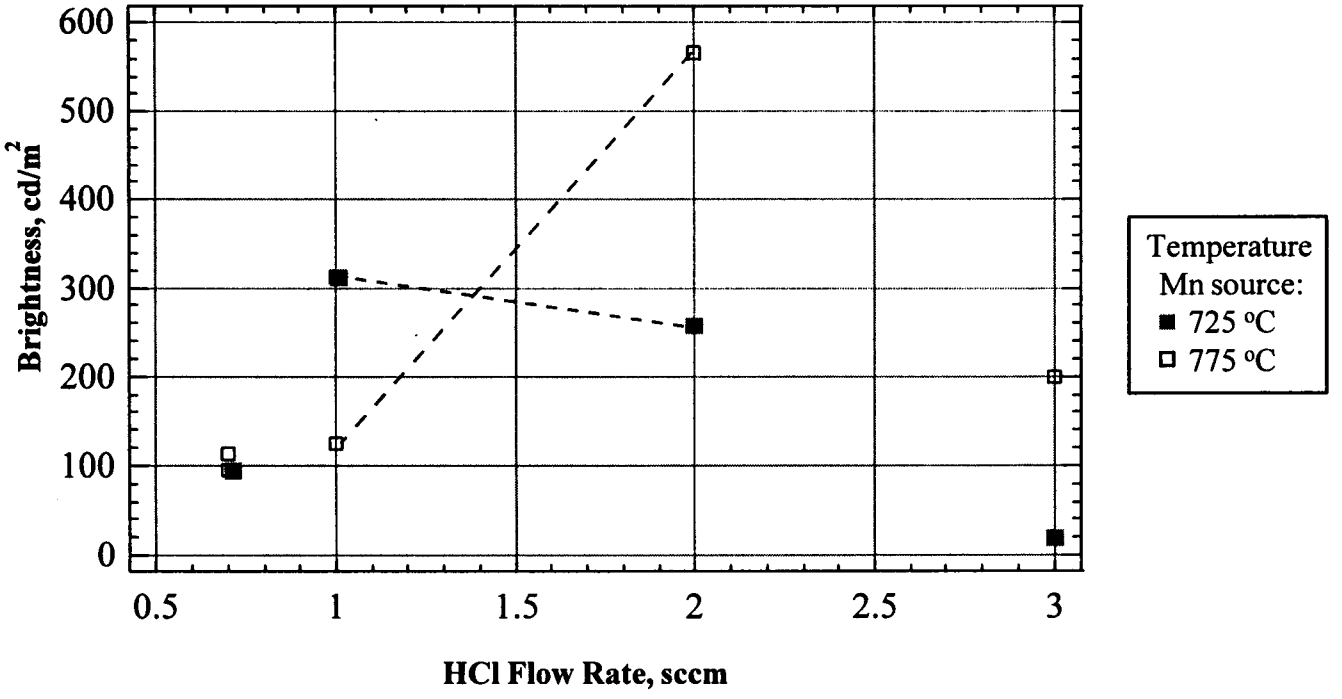

Figure 4-3. Plot of brightness of ACTFEL device versus HCl flow rate at substrate temperature of 550 °C.

Both the Mn source temperature and the HCl gas flow rate can affect the concentration of Mn, the luminescent center, in the growing film. Higher Mn source temperatures lead to faster reaction between HCl and Mn powder, and therefore, increase the $MnCl_2$ concentration transported to the growth surface. Higher HCl gas flow rates enhance the mass transport of HCl to Mn powder and also increase the $MnCl_2$ concentration transported to the growth surface. Brightness increases with Mn concentration as more luminescent centers are available to emit light. However, above a critical Mn concentration, non radiative relaxation processes between neighboring Mn ions dominate, and the luminescence decreases. This phenomena is known as concentration quenching. As can be seen from Figure 4-3, the effect of the Mn source temperature and the HCl gas flow rate on brightness is clearly more complicated than merely supplying Mn centers to the film. The highest brightness occurs at 775 ^{o}C Mn source temperature and 2 sccm HCl gas flow rate, which indicates that there is not yet enough Mn ions in the film for concentration quenching. However at the lower Mn source temperature, a higher brightness is obtained at 1 sccm HCl than 2 sccm. Since there are even less Mn incorporated at this source temperature, this decrease cannot be explained by concentration quenching. Clearly something else is going on. It may be that the HCl and $MnCl_2$ gases are supplying Cl to the growth surface which is then incorporated into the film. In fact, other work in our group has exploited Cl to obtain bright blue photoluminescence (PL) in ZnS films [Chen *at al*, 1998] and has explained unusual red PL spectra with a Cl related defect [Lu, 1999]. In order to elucidate the effect of these growth parameters on brightness, electrical characterization of ZnS:Mn ACTFEL devices is undertaken.

4.2 Electrical Characterization of HTCVD ZnS:Mn ACTFEL Devices

Figures 4-4 and 4-5 show C-V curves when the Al electrode is positively and negatively biased, respectively, of three samples that have low, medium, and high brightness. The curves are obtained at V_{max} (applied external voltage) equal to 20, 40, and 60 V above the threshold voltage. The arrows on the plot show an increasing V_{max}. Table 4-2 summarizes the total and insulator capacitance values for each sample. These films are labeled 15, 10, and 12 in the table and the figures according to their place in the design of experiment array. In addition to the samples' physical capacitance values, capacitance values obtained from C-V and Q-V curves are also reported here. The insulator capacitance values obtained from C-V and Q-V curves are the average values from the positive and negative polarities. The phosphor capacitances are calculated by Eqn. 2-4.

The medium and bright samples exhibit asymmetric behavior when comparing positive and negative polarities. They show a decrease in turn on voltage as V_{max} increases during the positive pulse (Figure 4-4). This behavior is typical of ACTFEL devices. At higher V_{max}, more conduction charge transports across the phosphor, leading to higher polarization charge. As discussed in Section 2.7, the electric field from the polarization charge enhances the phosphor field from the applied voltage. Therefore, as V_{max} increases, the necessary applied field component diminishes, and a lower turn on voltage results. The sample with low brightness and all samples during the negative portion of the wave form, however, exhibit, anomalous behavior where the turn on voltage increases as V_{max} increases. This behavior is very uncommon in ACTFEL devices and cannot be accounted for by the ideal phenomena described in Section 2.7. One possible origin for this behavior is space charge in the phosphor layer. This mechanism will be discussed further in Section 4.4.

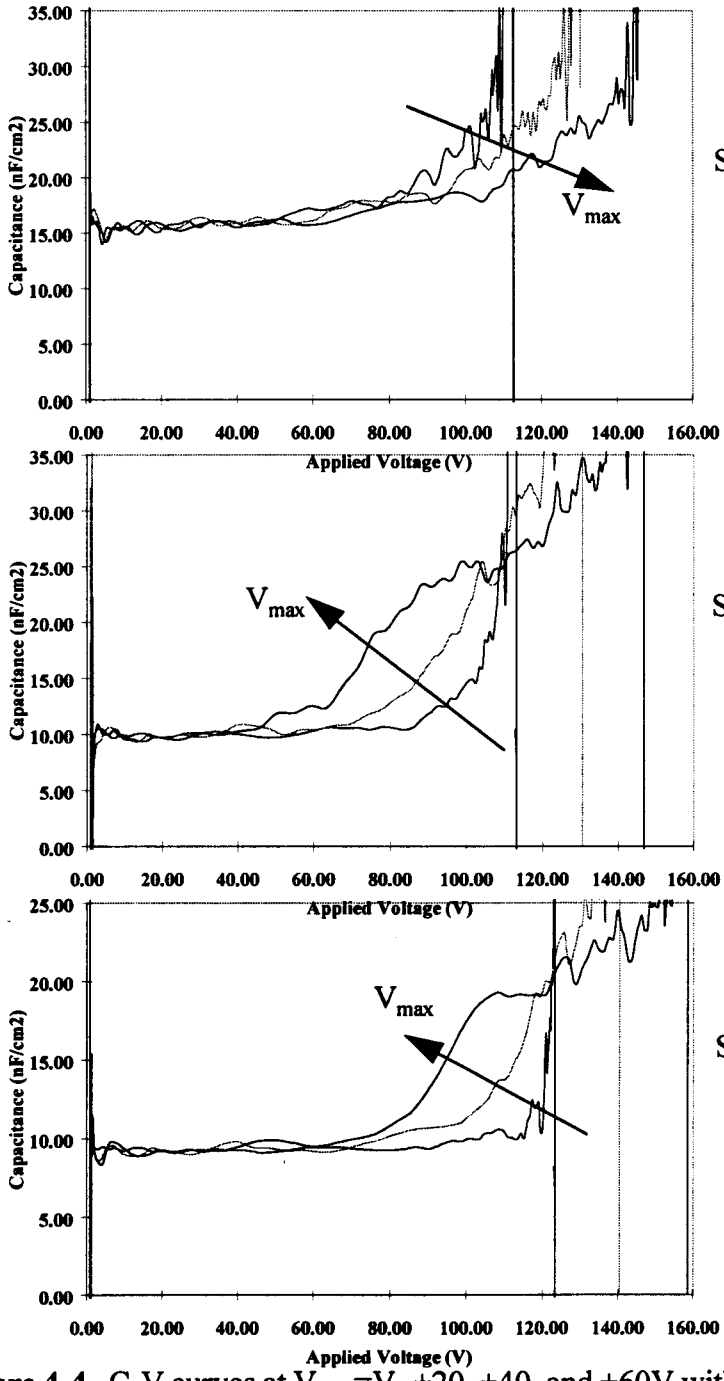

Figure 4-4. C-V curves at $V_{max}=V_{th}+20$, +40, and +60V with Al electrode positively biased, for device with (a) low, (b) medium, and (c) high brightness.

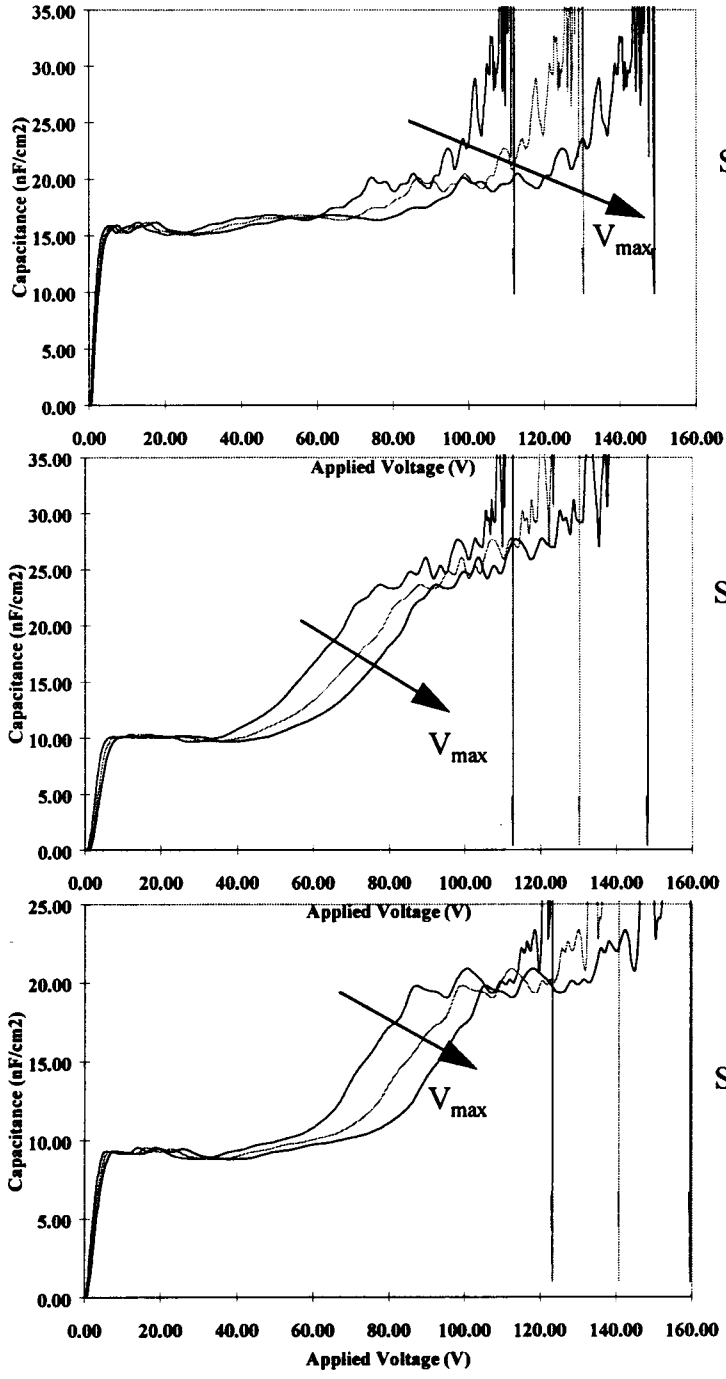

Figure 4-5. C-V curves at $V_{max}=V_{th}+20$, +40, and +60V with Al electrode negatively biased, for device with (a) low, (b) medium, and (c) high brightness.

Table 4-2. Total and insulator capacitances values for three samples which have different brightness.

Brightness	**Low**	**Medium**	**High**
Sample #	**15**	**10**	**12**
Brightness (cd/m^2)	69	210	584
C_t-physical	7.2	7.2	7.2
C_t-C-V	15.6	10	9.2
C_t-Q-V	15.6	10.2	9.2
C_i-physical	17.6	17.6	17.6
C_i-C-V	N/A	25	19.6
C_i-Q-V	21.7	25.7	20.2
C_p-physical	12.2	12.2	12.2
C_p-C-V	N/A	16.7	17.3
C_p-Q-V	55.5	16.9	16.9

C = capacitance (nF/cm^2)

Table 4-2 shows the measured values of total capacitance ($C_{total}^{meas.}$), insulator capacitance ($C_i^{meas.}$), and phosphor capacitance ($C_p^{meas.}$) from C-V (and Q-V) measurements are higher than their physical values: $C_{total}^{phy.}$, $C_i^{phy.}$ and, $C_p^{phy.}$. As device brightness increases, the value of $C_{total}^{meas.}$ decreases, becoming closer to the physical value. The discrepancy between measured and physical capacitances can also be an indication of space charge [Thuemler, 1998]. These data indicate that the brighter devices have less space charge. The C-V curves in Figures 4-4 and 4-5 also exhibit overshoot, also an indication of space charge creation in the phosphor layer.

Furthermore, a flat C_i portion is absent from several of the C-V curves. The insulator capacitance from the C-V measurement in Figures 4-4 (a) and 4-5 (a) is impossible to define because of the absence of the flat C_i portion. Some curves are not well defined when the V_{max} is close to V_{th}, i.e., $V_{max}=V_{th}+20V$, such as in Figures 4-4 (b) and (c). This ill defined flat C_i portion of C-V curve is attributed to the insufficient

conduction current to completely shunt the phosphor capacitance [Thuemler, 1998]. In this case, the assumption of constant phosphor field during the portion of the waveform right after turn on (as presented in Section 2.7) is no longer valid.

Figures 4-6 and 4-7 show Q-V and Q-F_p curves, respectively, for the same three samples discussed above. The arrows on the plots indicate increasing V_{max} at 20, 40 and 60V above the threshold voltage. The C_t and C_i values on Figure 4-6 are obtained by best fitting the AB and BC portions of the curve, respectively.

Figure 4-7 (a) shows the steady-state phosphor electric field is never attained, as the BC portion of the Q-F_p curves is never vertical. The leakage charge at 60 V above the threshold voltage is so great that the polarization charge and phosphor field is identical to that at 40 V above the threshold voltage. Figure 4-7 (a) also shows there is a field relaxation in the BC portion of the curves. This field relaxation in early portion of the applied waveform is an additional indication of the existence of space charge generation in the device.

Figures 4-6 (b) and 4-7 (b) shows Q-V and Q-F_p curves, respectively, for a HTCVD ACTFEL device which has medium brightness (210 cd/m^2). The Q-F_p curve at 60V above the threshold voltage in Figure 4-7 (b) shows asymmetrical field clamping. The field is clamped only during the positive polarity of the applied waveform. This observation is supported by the lack of sharp change in the slopes in the negative polarity portion of Q-V curves in Figure 4-6 (b).

An interesting phenomenon manifests at the onset of the negative pulse in the Q-F_p curves of all three devices. The polarization charge actually becomes more positive, initially as the field increases. The increase in polarization charge opposes the direction that charges want to flow in the field. This phenomenon is greatest in the device that has the lowest brightness. At the onset of the positive pulse, on the other

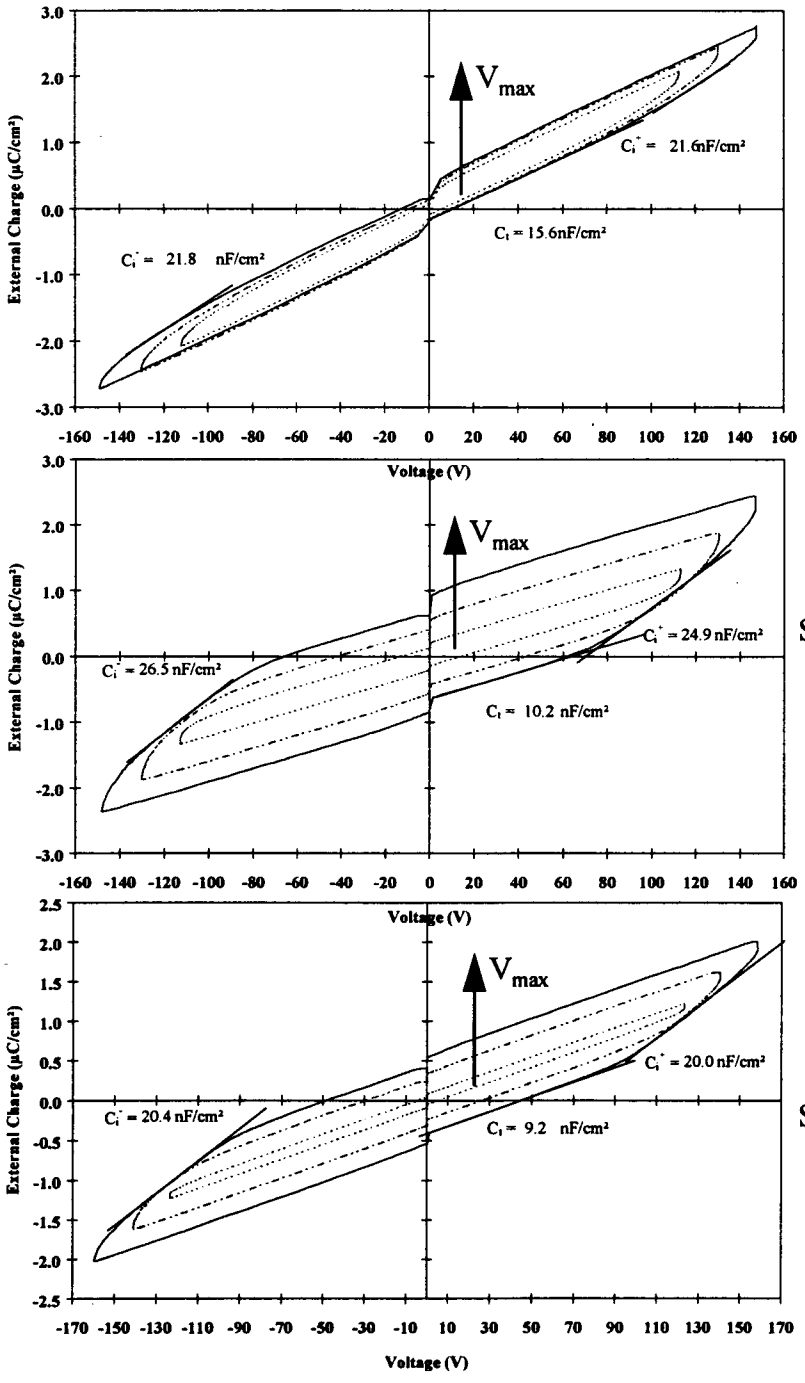

Figure 4-6. Q-V curves at $V_{max}=V_{th}+20$, +40, and +60V for device with (a) low, (b) medium, and (c) high brightness.

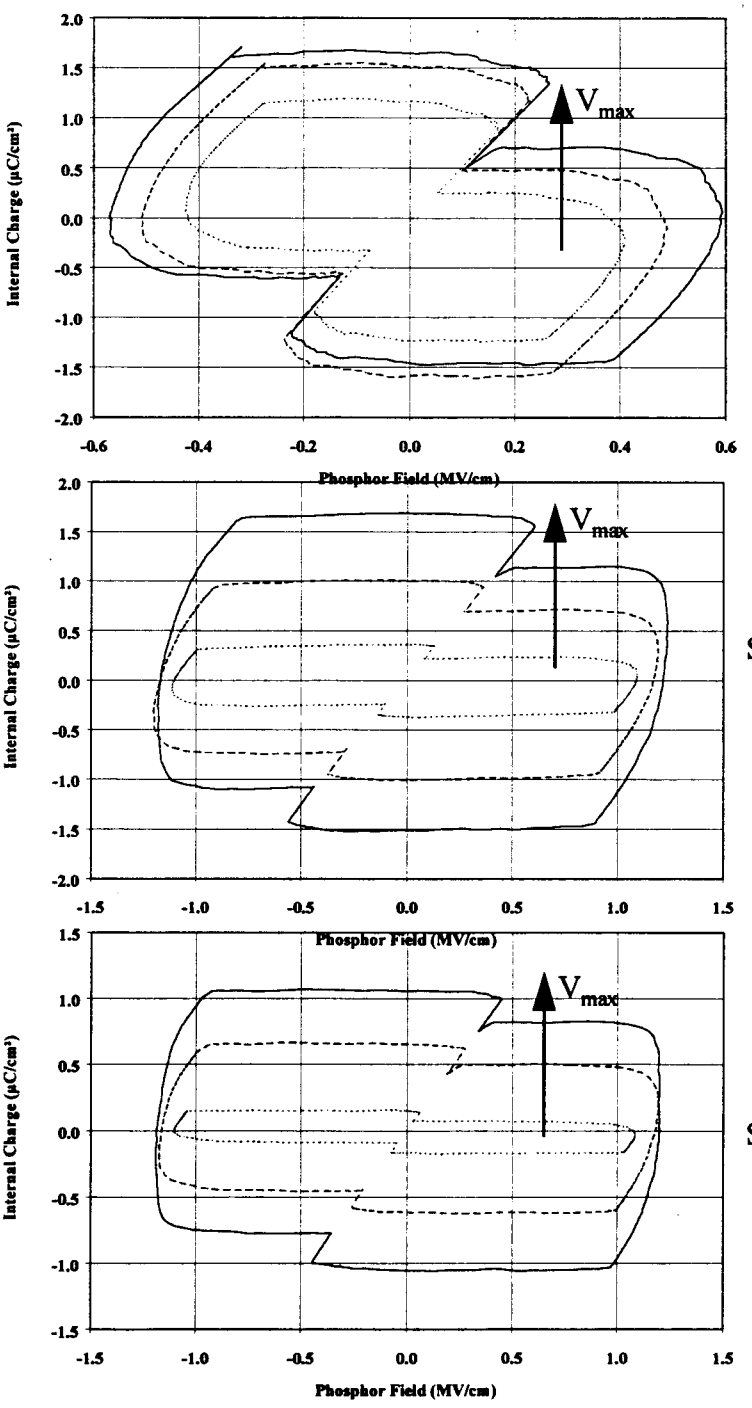

Figure 4-7. Q-F_p curves at $V_{max}=V_{th}+20$, +40, and +60V for device with (a) low, (b) medium, and (c) high brightness.

hand, behavior is typical of an ACTFEL device where the polarization charge remains constant as the field builds (as discussed in Section 2.7).

Table 4-3 summarizes internal charges obtained from Q-F_p measurement for the three samples mentioned earlier. Ironically the device with high brightness (sample #12) has the lowest conduction charge.

In summary, two major effects are revealed by electrical characterization:

1. The devices exhibit **asymmetric** behavior when comparing positive and negative pulses. This effect is exhibited by the shift in turn on voltage with V_{max}, in the anomalous rise in polarization charge at the onset of the negative pulse, and in field clamping.
2. These devices show evidence of **space charge** in the phosphor bulk. The amount of space charge appears to be greatest for the sample with lowest brightness.

Table 4-3. Q-F_p measurement results for three samples which have different brightness.

Charge ($\mu C/cm^2$)	Brightness		
	Low (sample #15)	**Medium (sample #10)**	**High (sample #12)**
Q^+_{cond}	2.27	2.77	1.84
Q^-_{cond}	2.20	2.63	1.89
Q^+_{pol}	0.72	1.15	0.83
Q^-_{pol}	0.60	1.08	0.78
Q^+_{relax}	1.13	1.00	0.56
Q^-_{relax}	1.07	1.13	0.65
Q^+_{leak}	0.97	0.38	0.24
Q^-_{leak}	0.86	0.42	0.28

It is possible that both these effects can be related to incorporation of Cl that was suggested in Section 4.1.

4.3 Brightness Transient (Decay Time) Measurements

In this section, the results of brightness-voltage and brightness transient (decay time) measurements of HTCVD ACTFEL samples that are not used in the DOE study are discussed. These data are included because they provide additional information about asymmetrical behavior in these devices. The data are summarized in Figure 4-8 and Table 4-4. In Figure 4-8, decay times of both positive and negative pulses are plotted versus device brightness. Four samples have been grown in a H_2S environment. The decay times for these films are indicated by open squares and triangles. These films have a cubic crystal structure and show a preferred orientation in the (311) direction. The one sample grown without H_2S present is represented by filled symbols. It has a hexagonal structure and growth occurs predominately along the (002) direction. The (311) growth plane is less dense than the close packed (002) plane. The difference between decay time of positive pulse and that of negative pulse is shown in Table 4-4, under column marked "Δ Decay Time." In all cases the decay time during the negative pulse is very fast and significantly less than the decay time after the positive pulse. The film without H_2S present shows the smallest Δ Decay Time.

Also plotted in Figure 4-8 is FWHM (full width at half maximum) values from X-ray diffraction (XRD) data obtained by Chen [1998]. FWHM values give an indication of the average grain size in ZnS:Mn film and the overall ZnS:Mn film quality. The grain size is inversely proportional to the FWHM value. A FWHM of 0.125 (the lowest value) corresponds to a crystallite size of 64 nm when the film thickness is around 6000 Å. As these data indicate most of these films have grains of comparable size.

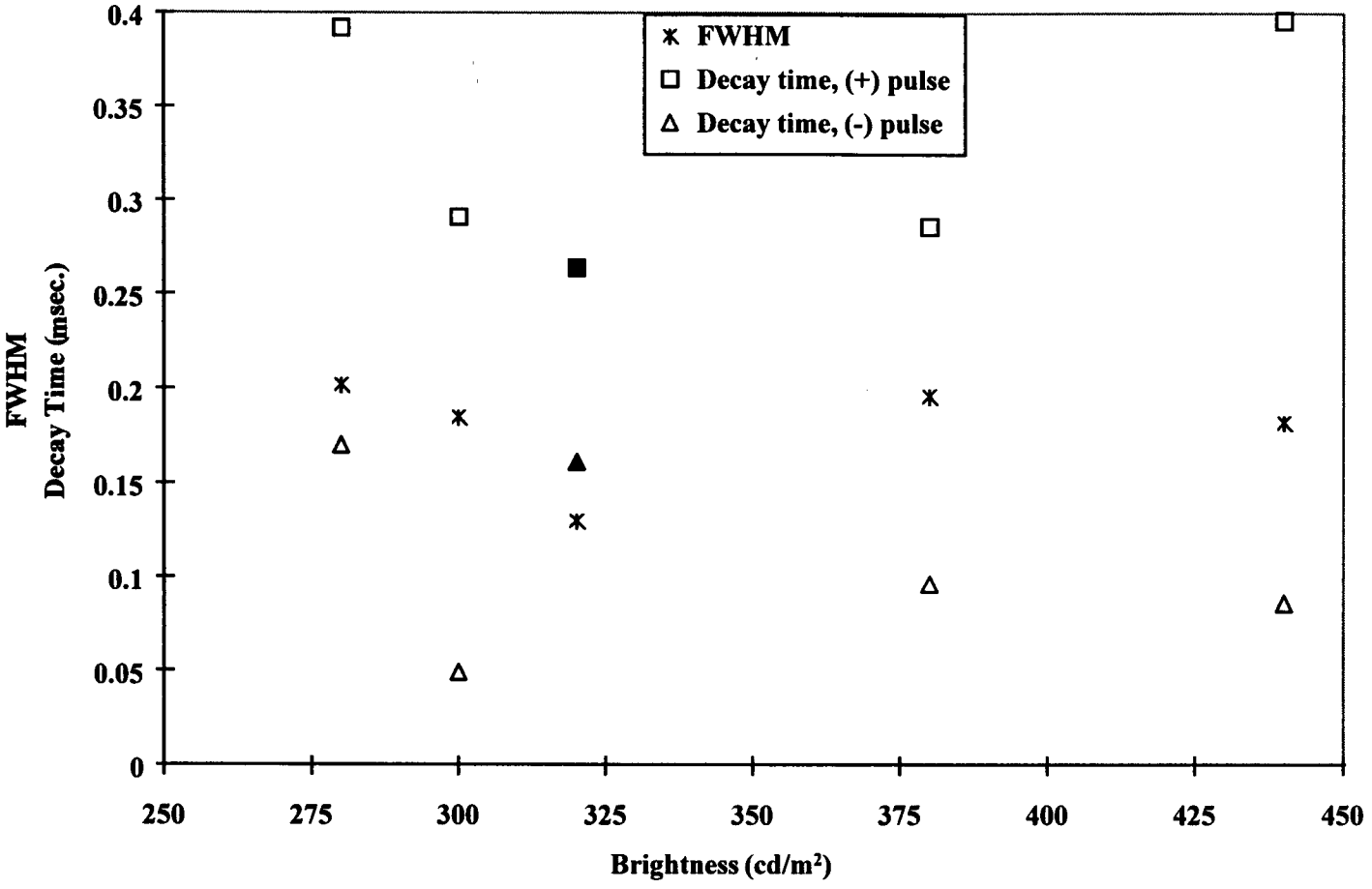

Figure 4-8. Brightness vs. FWHM and Decay Time (filled sysmbols indicate ZnS:Mn film was deposited without H_2S).

Table 4-4. Relations between device brightness with decay time and internal charges.

#	Brightness (cd/m^2)	Δ Decay Time (msec.)	Conduction Charge (nF/cm^2)	Polarization Charge (nF/cm^2)	Relaxation Charge (nF/cm^2)	Leakage Charge (nF/cm^2)
1	280	0.22	4.10	1.85	1.77	0.31
2	300	0.24	4.67	2.29	1.51	0.10
3*	320	0.10	2.35	0.95	0.77	0.47
4	380	0.19	5.54	2.67	2.54	0.14
5	440	0.31	3.60	1.68	1.03	0.22

* indicate ZnS:Mn was deposited without H_2S

Decay time measurements give an indication of Mn relaxation processes. Long decay times indicate radiative relaxation (and light emission). On the other hand, short decay times occur when non-radiative processes are available. For example, in concentration quenching, excited Mn relaxes non radiatively through Mn-Mn dipolar interactions. In fact, if this process is the dominant non-radiative relaxation mechanism, decay times can be used to estimate Mn concentration. These data suggest that non-radiative relaxation is more prevalent during the negative pulse.

Table 4-4 also includes values of internal charges obtained from Q-F_p curves. The films grown in the less dense (311) direction exhibits relatively large conduction charge. Therefore, more electrons are available to excite luminescent centers; however, the brightness in not significantly changed.

4.4 Proposed Cl Defect Model

As discussed in section 4.1, incorporation of Cl into the growing ZnS:Mn film provides a possible explanation for the interaction between Mn source temperature and HCl flow rate. We propose that a Cl defect is also consistent with the anomalous electrical data presented in Sections 4.2 and 4.3. In order to investigate this hypothesis,

we must first determine where the Cl defect sits in the film. Three possible sites include: substitution of a sulfur in the crystal lattice, in an interstitial site, or preferential precipitation along the grain boundaries of the polycrystalline film. While the first alternative is commonly cited in other ACTFEL systems, it is inconsistent with our data. If Cl were to sit in an S site, we would expect less Cl to be incorporated when grown in an H_2S environment. However, the asymmetric decay times, which we are attributing to a Cl defect, are largest for this case. In order to distinguish between the latter two possibilities, it is instructive to look at the morphology of the growing film.

The cross-sectional image of a ZnS:Mn film obtained by Transmission Electron Microscopy (TEM) is shown in Figure 4-9 (a). These photographs are at 100,000X magnification. The white region between the two films is epoxy that is used to prepare the cross section. The figure shows the grains are smaller at the ITO/ATO interface and larger at the growth surface. The average grain size is around 100-200 nm. Hence the grain boundaries are physically asymmetrical being concentrated at the initial growth interface. Thus a Cl defect precipitated at the grain boundary would be favored at the initial growth interface. On the other hand, if Cl sat in an interstitial crystal site, it should have a relatively even distribution across the film. Furthermore the increased the asymmetric decay times when grown in an H_2S environment are consistent with Cl defect at grain boundaries. These films grow along the less dense (311) crystal plane and would have more opportunity to nucleate a Cl related defect. We propose this defect could then diffuse (or migrate) along the grain boundaries and possibly into the bulk crystal.

A schematic cartoon of the proposed Cl defect is presented in Figure 4-9 (b). It is preferentially located at the growth surface where the density of grain boundaries is high. To the right of the schematic, the directions of electron transport as a function of voltage polarity is also shown. During a positive pulse, electrons travel from the

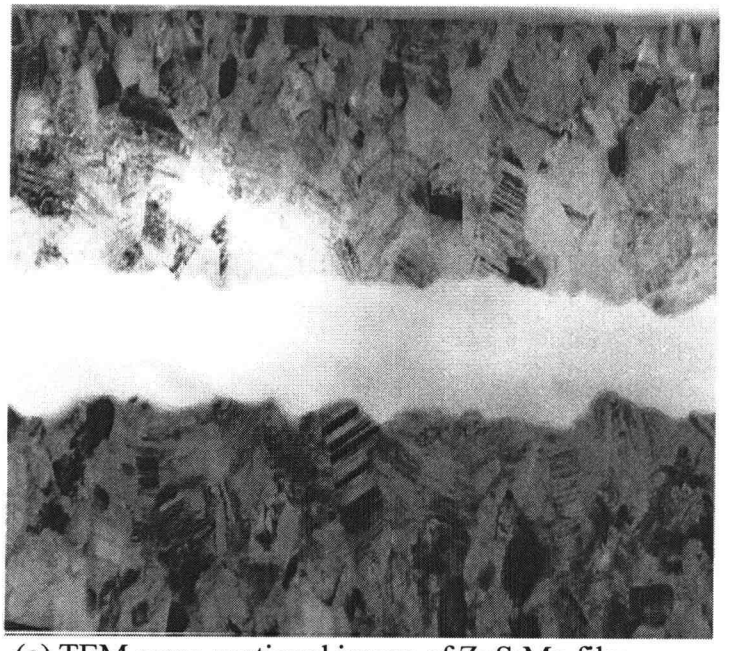

(a) TEM cross-sectional image of ZnS:Mn film

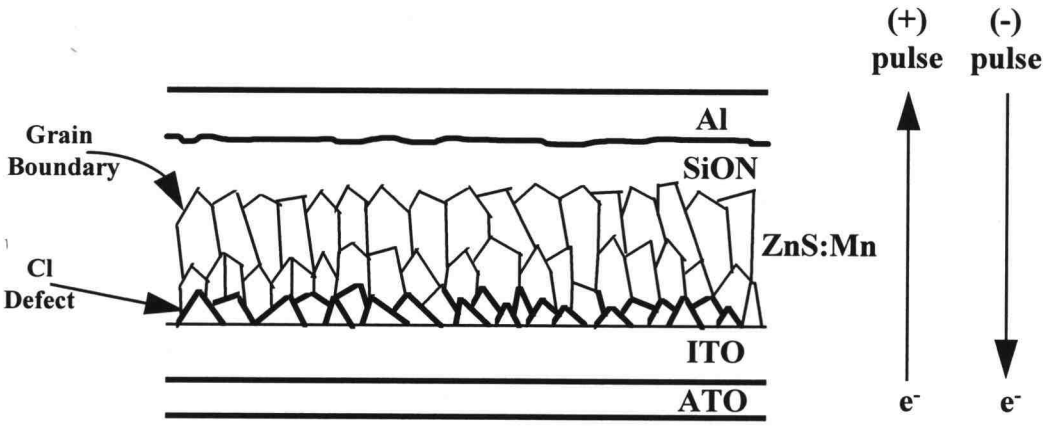

(b) schematic of the proposed Cl defect

Figure 4-9. (a) TEM crosss-sectional image of ZnS:Mn film [Chen, 1998] and (b) schematic of the proposed Cl defect.

substrate (ITO/ATO) toward the larger grains while they are directed towards the smaller grains (and the majority of the Cl defects) during the negative pulse. This viewpoint will be useful when reconciling the Cl defect model to the anomalous electrical behavior.

In Figure 4-5, an increase in turn-on voltage with V_{max} was demonstrated. This behavior can be explained by the negative charging of Cl defects close to the ATO surface. We believe the defect will easily form negative charge in order to fill its valence shell; however, there is no independent evidence of negative space charge. Figure 4-10 qualitatively shows the effect of negative charged Cl defects close to the ATO surface in the context of the discussion in Section 2.7. The dashed line represents the ideal case while the solid line shows the voltage distribution when the Cl defect is present. During a negative pulse (Fig 4-10 (a)), positive polarization charge exists at the ATO/phosphor interface. In this case, the negative space charge from the Cl defect opposes the effect of the polarization charge. Hence a larger field component from the applied voltage is required to initiate conduction of electrons. If the Cl charging is a dynamic process, this negative charge will be larger for larger applied voltages (with their larger conduction charges). Hence the turn on voltage will increase with V_{max}. On the other hand, a pulse of positive polarity has negative polarization charge at the ATO/phosphor interface. The negative space charge now enhances the field, reducing the turn on voltage. Neutral Cl defects (in the case where they are all dynamically discharged) would show the same trend. The low brightness film shows an increase in turn on voltage with both polarities. This film was deposited at very large HCl flow rate (3 sccm) and low substrate temperature (470 °C). Hence it is likely to have extensive Cl incorporation and small grains. Thus the shift in turn-on voltage described above could be present at both interfaces. We believe the anomalous effect noted in the Q-F_p plots could be related to the dynamic charging of these defects.

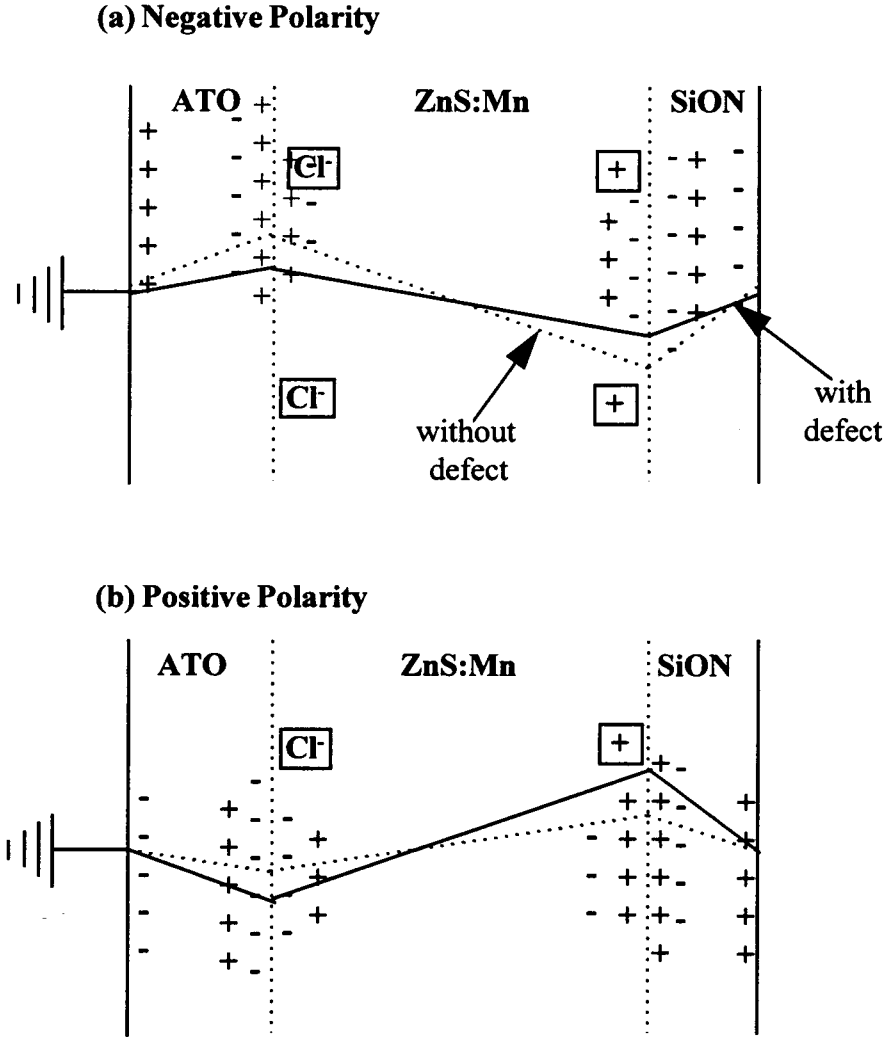

Figure 4-10. Effect of Cl defect on polarization charge during (a) negative polarity and (b) positive polarity

The Cl defect model is also consistent with the decay time asymmetries discussed in Section 4.3. The decay time is significantly larger for the positive pulse than the negative polarity. As Figure 4-10 (b) shows, a negative pulse sends electrons towards the ATO interface. Since the electrons which are accelerated by the applied field need to travel a distance before they have enough energy to excite a luminescent center, the phosphor closest to the injection interface is not excited. Hence, the smaller grains become more dominant in their contribution to the luminance. These grains are associated with Cl defects which can lead to non-radiative relaxation processes which are very fast. During a positive pulse, the Mn in the larger grains are excited. There are not defects associated with this region and slower, radiative emission can be realized.

4.5 Processing Solution to Remove Cl Defects

Since the defects are believed to originate from the nucleation of Cl at high grain boundary density, one potential solution is to remove the Cl source as the grains begin to grow and only later expose the film to Cl. Three such films were grown in this manner. All were grown without H_2S present to increase the density of the growth plane. The first film was grown for 1.5 hours before turning on the HCl gas. The next two were grown for 0.75 hours before turning on HCl. The total deposition time in all three cases was 3 hours. Summary data for these three films are also presented in Table 4-5. Brightness-voltage plots for these three films are shown in Figure 4-11. All films show significantly greater brightness than those deposited in the DOE. Decay time measurements for sample #2 is shown in Figure 4-12. Both polarities are comparable. In fact, now the decay time for the negative pulse is greater. Furthermore,

Table 4-5. Summary of process conditions and B-V and B-T results of films grown without HCl first.

#	Time w/o HCl (hours)	Time w/ HCl (hours)	HCl Flow Rate (sccm)	Substrate Temperature (°C)	Maximum Brightness (cd/m^2)	(+) pulse Decay Time (msec.)	(-) pulse Decay Time (msec.)	Δ Decay Time (msec.)
1	1.5	1.5	1.0	500	850	0.15	0.25	-0.10
2	0.75	2.25	1.0	500	608	0.12	0.18	-0.06
3	0.75	2.25	0.5	550	1470*	0.27	0.19	0.08

* maximum brightness achieved higher than shown in Figure 4-11 ($V_{appl.}$>200 V).

the decay times for both polarities are smaller than the optimum value (0.6 msec. [Mikami, 1991]) suggesting a high Mn concentration in the film. After both the positive and negative pulses, there occurs a second peak after the maximum peak. The second peaks are at ± 50 μsec after the pulses started, just after the applied voltage goes back to zero. This phenomenon may be caused by the release of a electron by Cl defects (negative space charge). Instead of flowing in the direction toward the positively biased electrode, these electrons flow in the opposite direction. The electron flow is caused by the established field caused by polarization charge and enhanced by the negative space charge. This process is similar to the leakage charge process however the electrons are from Cl defects instead of from the interface. Hence these electrons reduce the established polarization charge at the interfaces. These electrons will gain enough energy to impact and excite Mn centers. It is not clear at this point what exactly is causing the release of electron by Cl defects.

The Sample #3 was deposited with a lower HCl gas flow rate, to reduce Mn concentration, and higher substrate temperature to improved film crystal quality. As a result, we obtained a sample with much higher brightness but also a higher threshold voltage because the film is thicker.

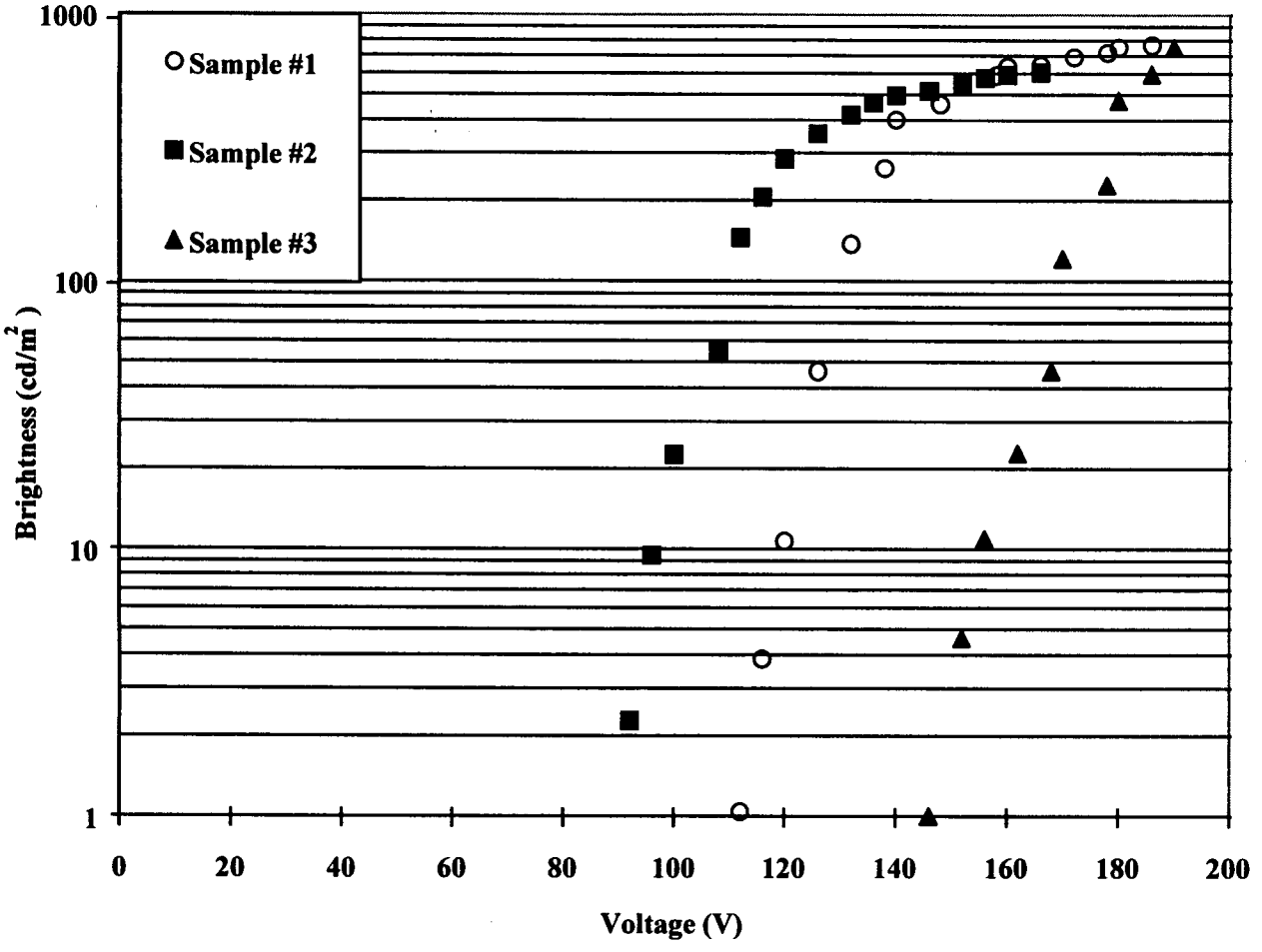

Figure 4-11. Brightness-voltage plots for 3 samples grown without HCl at the beginning of deposition.

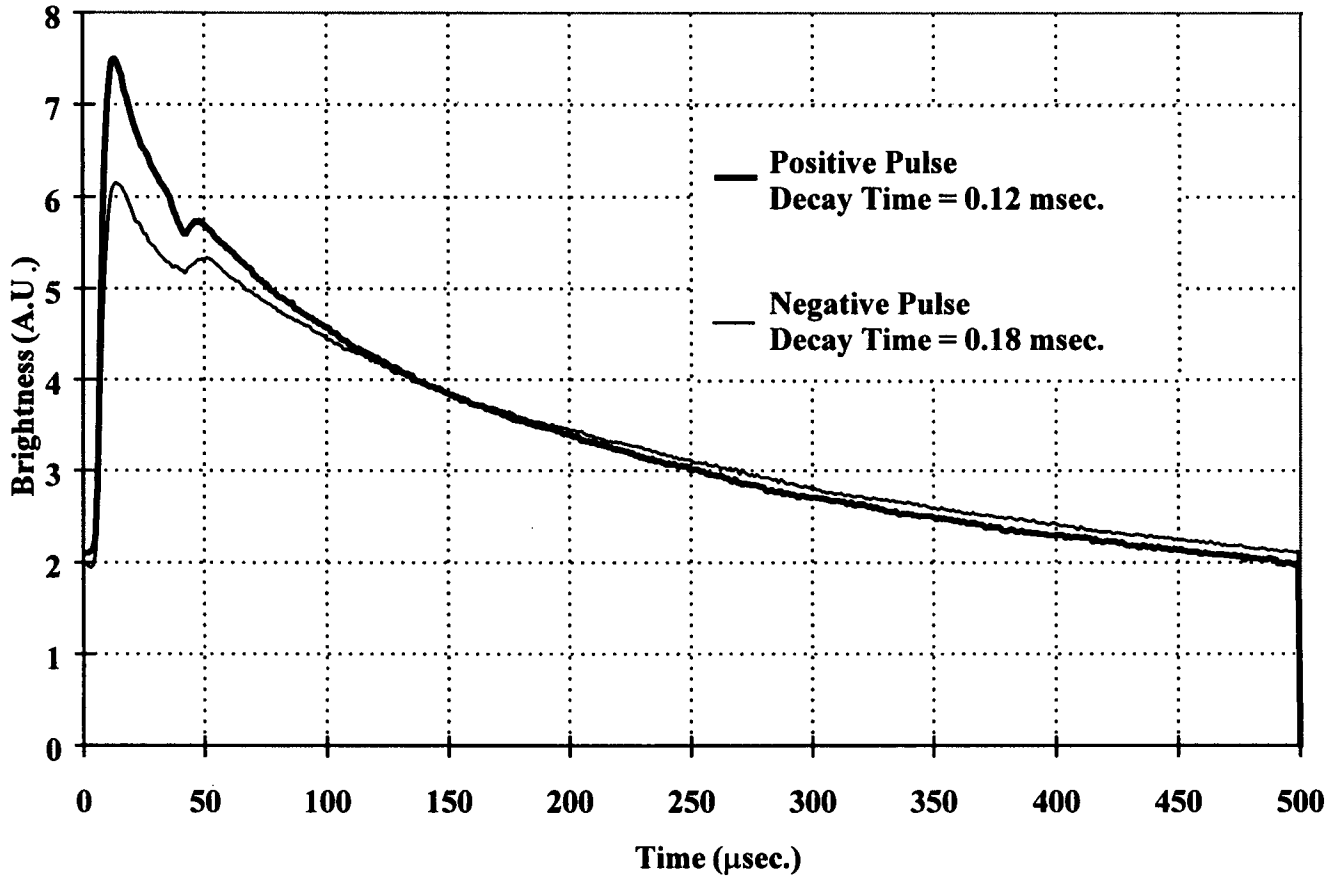

Figure 4-12. Brightness intensity vs. time for positive and negative pulses.

The Q-V and Q-F_p curves for sample #1 are shown in Figure 4-13. Both plots depict strong field clamping for both positive and negative polarity of the applied waveform. The measured insulator capacitance values, obtained from the Q-V curve, for both positive and negative pulses are comparable. Furthermore, the Q-F_p curves in Figure 4-13 (b) do not exhibit the anomalous behavior at the onset the negative pulse. Overall we can conclude that this device exhibit a symmetrical electrical behavior when comparing the positive and negative pulses.

While film growth without HCl present leads to brighter films, it is a sub-optimal solution. Part of the ZnS host does not have luminescent centers. In fact the brightness of these films is less than state-of-the-art devices by a factor of 2-3. In these films, the Mn concentration has not been optimized; however it is believed other processing solutions need to be realized to make the HTCVD system viable.

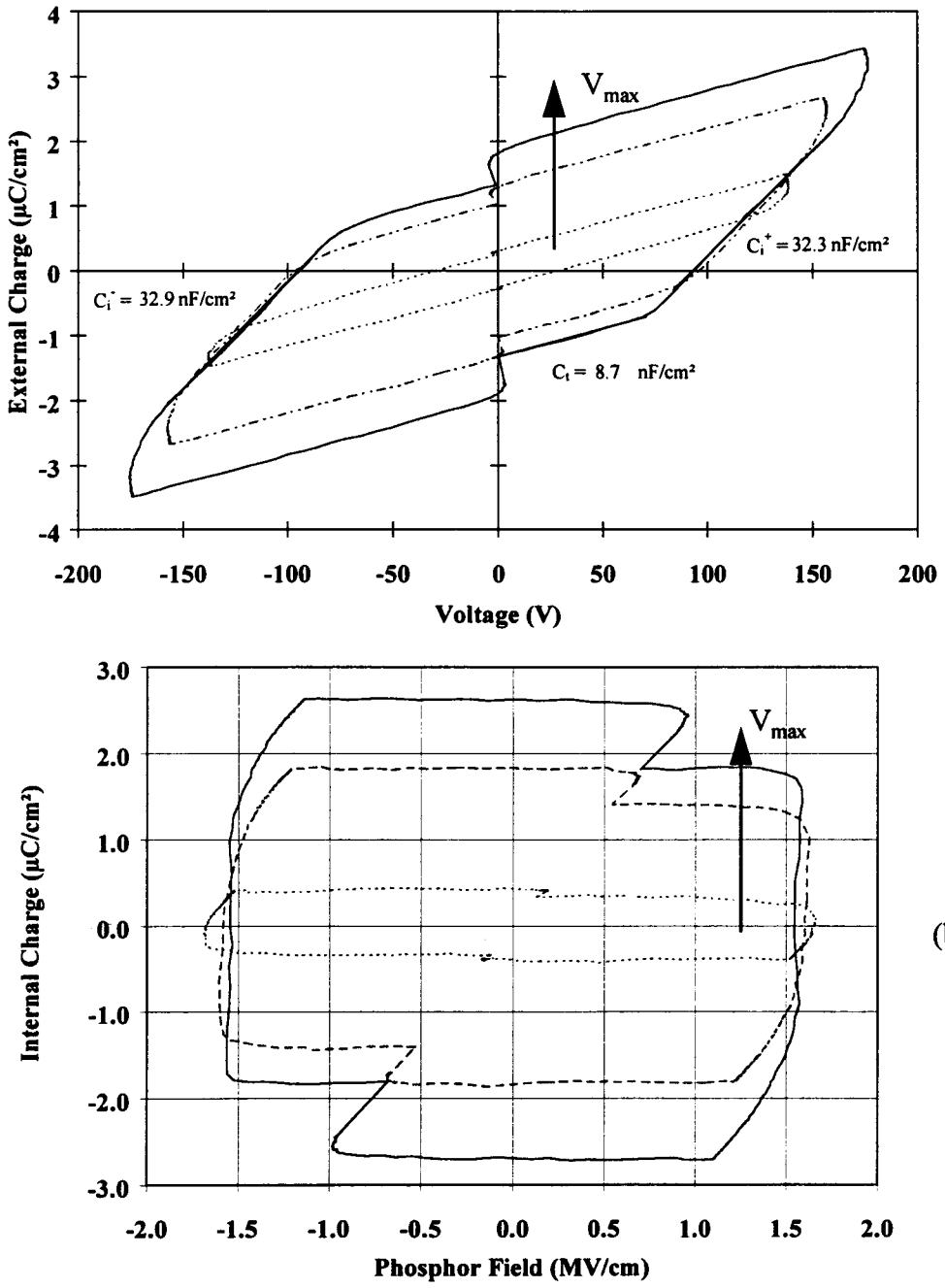

Figure 4-13. The (a) Q-V and (b) Q-F_p curves at V_{max}=V_{th}+20,+40, and 60V for the device grown initally without HCl gas.

Chapter 5

CONCLUSION

Process development of ZnS:Mn deposition using halide transport chemical vapor deposition (HTCVD) has been studied. To this end, electrical characterization of HTCVD ZnS:Mn ACTFEL devices also has been used. Process optimization focused on a simple design of experiment (DOE) with the brightness of the ACTFEL device as the major response. An ideal model of the electrical characteristics of a ZnS:Mn ACTFEL device was developed in order to understand the results of the electrical characterization of real HTCVD ZnS:Mn ACTFEL devices.

Statistical analysis (ANOVA) of brightness-voltage measurement shows ZnS source temperature and H_2S gas flow rate effects are insignificant and indistinguishable from the experimental error. The substrate temperature and HCl gas flow rate have a strong effect. The Mn source temperature also influences brightness. The highest brightness is achieved when the phosphor layer is deposited at a substrate temperature of 550 ^{o}C. The HCl gas flow rate and Mn source temperature show strong interaction. The brightness is not directly related to the Mn concentration in the films. It is proposed that the HCl and $MnCl_2$ gases are supplying Cl to the growth surface which is then incorporated into the film.

In order to elucidate the effect of these growth parameters on brightness, electrical characterization and brightness transient measurements of ZnS:Mn ACTFEL devices are undertaken. Three major effects are revealed:

1. The devices exhibit **asymmetric** behavior when comparing positive and negative pulses. This effect is exhibited by the shift in turn on voltage with

V_{max}, in the anomalous rise in polarization charge at the onset of the negative pulse, and in field clamping.

2. These devices show evidence of **space charge** in the phosphor bulk. The amount of space charge appears to be greatest for samples with low brightness.
3. The devices exhibit **asymmetric** decay time when comparing positive and negative polarities. In all cases the decay time during the negative pulse is very fast and significantly less than the decay time after the positive pulse. The largest difference in decay time is shown by films deposited in an H_2S environment.

It is proposed that these effects are related to incorporation of Cl into the ZnS:Mn film. Cross-sectional images obtained by Transmission Electron Microscopy (TEM) shows the grains are smaller at the ITO/ATO interface and larger at the growth surface. Hence the grain boundaries are physically asymmetrical and a Cl defect precipitated at the grain boundaries is proposed. This defect could then diffuse (or migrate) along the grain boundaries and possibly into the bulk crystal. A Cl defect model is consistent with anomalous electrical behavior that is observed.

Since Cl defects are believed to originate from the nucleation of Cl at high grain boundary density, one potential solution is to remove the Cl source as the grains begin to grow and only later expose the film to Cl. Samples grown in this manner show significantly greater brightness than those deposited in the DOE. Decay time of these samples are comparable for both polarities; however Mn concentration was not optimized. While film growth without HCl present at the beginning of deposition leads to brighter films, it is a sub-optimal solution. Part of the ZnS host does not have luminescent centers. In fact the brightness of these films are less than state-of-the-art

devices by a factor of 2-3. It is believed other processing solutions need to be realized to make the HTCVD system viable.

NOMENCLATURE

List of Abbreviations

AC	Alternating-Current
ACTFEL	Alternating-Current Thin Film Electroluminescent
ALE	Atomic Layer Epitaxy
ANOVA	Analysis of Variance
ATO	Aluminum Titanium Oxide
BTO	Barium Tantalite
B-T	Brightness-Transient
B-V	Brightness-Voltage
C-V	Capacitance-Voltage
CVD	Chemical Vapor Deposition
DOE	Design of Experiment
EBE	Electron Beam Evaporation
EL	Electroluminescent
FED	Field Emission Display
FWHM	Full Width at Half Maximum
HTCVD	Halide Transport Chemical Vapor Deposition

ITO	Indium Tin Oxide
LCD	Liquid Crystal Display
MOCVD	Metal-Organic Chemical Vapor Deposition
MSD	Multi-Source Deposition
PECVD	Plasma Enhanced Chemical Vapor Deposition
PL	Photoluminescence
PVD	Physical Vapor Deposition
Q-F_p	Internal Charge-Phosphor Field
Q-V	External Charge -Applied Voltage
SID	Society on Information Display
TEM	Transmission Electron Microscopy
XRD	X-ray Diffraction

List of Symbols

ΔV_i	Voltage drop across dielectric *i*
ΔV_{pol}^{i}	Voltage drop caused by polarization charge across dielectric *i*
ΔV_{tot}^{i}	Voltage drop caused by total potential across dielectric *i*
ε_o	Permitivity of free space
ε_r	Dielectric constant

C_i	Insulator capacitance
C_i	Capacitance of dielectric *i*
$C_i^{meas.}$	Measured values of insulator capacitance
$C_i^{phy.}$	Physical value of insulator capacitance
C_{ib}	Capacitance of the bottom insulator layer
C_{it}	Capacitance of the top insulator layer
C_p	Phosphor capacitance
$C_p^{meas.}$	Measured values of phosphor capacitance
$C_p^{phy.}$	Physical value of phosphor capacitance
C_{sense}	Sense capacitor
C_t	Total capacitance
$C_{total}^{meas.}$	Measured values of total capacitance
$C_{total}^{phy.}$	Physical value of total capacitance
Df	Degrees of freedom
d_i	Thickness of dielectric *i*
d_p	Thickness of phosphor film
E	Electric field
E_{appl}	Electric field caused by applied voltage
E_f	Fermi level

E_i	Electric field of dielectric *i*
E_{pol}	Electric field caused by polarization charge
E^i_{tot}	Electric field in dielectric *i* caused by total potential
E_{total}	Electric field caused by total potential
F_p	Phosphor field
F_{ss}	Steady state phosphor field
i	Any dielectric in the stack (ATO, ZnS:Mn or SiON)
Q_{appl}	Charge caused by applied potential
Q_i^{dis}	Displacement charge of dielectric *i*
Q^e	External charge
Q_{cond}	Conduction charge
Q^+_{cond}	Conduction charge of positive polarity
Q^-_{cond}	Conduction charge of negative polarity
Q_{leak}	Leakage charge
Q^{e+}_{leak}	External leakage charge of positive polarity
Q^{e-}_{leak}	External leakage charge of negative polarity
Q_{pol}	Polarization charge
Q^{e+}_{pol}	External polarization charge of positive polarity
Q^{e-}_{pol}	External polarization charge of negative polarity

Q_{relax}	Relaxation charge
Q^{+}_{relax}	Relaxation charge of positive polarity
Q^{-}_{relax}	Relaxation charge of negative polarity
Q^{i}_{pol}	Polarization charge of dielectric *i*
Q_{ss}	Interface state density
Q^{i}_{tot}	Charge in dielectric *i* caused by total potential
V_{appl}	External applied potential
V_{th}	Threshold voltage
V_{to}	Turn-on voltage
V_{max}	Maximum applied voltage

REFERENCES

Abu-Dayah, A. I., "Internal charge-phosphor field analysis, electrical characterization, and aging studies of AC thin-film electroluminescent devices", M.S. Thesis, Oregon State University, 1993.

Abu-Dayah, A. I., J. F. Wager, and S. Kobayashi, "Internal charge-phosphor field characteristics of alternating-current thin-film electroluminescent devices", *Applied Physics Letter*, **62**, 744 (1993).

Barrow, W., R. Coovert, E. Dickey, T. Flegal, M. Fullman, C. King, and C. Laakso, *Conference Record of the 1994 International Display Research Conference*, 448 (1994).

Bringuier, E., "Charge transfer in ZnS-type electroluminescence", *Journal of Applied Physics*, **66**, 1314 (1989).

Chen, C., "A study of ZnS:Mn electroluminescent phosphors grown by halide transport chemical vapor deposition", M.S. Thesis, Oregon State University, 1998.

Chen, C., S. Husurianto, X. Lu, M.D. Koretsky, "The effect of processing conditions on crystal orientation and structure in ZnS:Mn thin films", *Journal of the Electrochemical Society*, **145**, 226 (1998).

Davidson, J. D., "Capacitance-voltage analysis, SPICE modeling, and aging studies of AC thin-film electroluminescent devices", M.S. Thesis, Oregon State University, 1991.

Davidson, J. D., J. F. Wager, R. I. Khormaei, C. N. King, and R. Williams, " Electrical characterization and modeling of alternating-current thin-film electroluminescent devices", *IEEE Transactions on Electron Devices*, **39**, 1122 (1992).

Destriau, G., "Recherches sur les Scintillations des Zinc aux Rayons", *Journal deChime Physique*, **33**, 587 (1936).

Douglas, A. A., "Alternating-current thin-film electroluminescent device physics and modeling", M.S. Thesis, Oregon State University, 1993.

Fowlkes, W. Y. and C. M. Creveling, "Engineering methods for robust product design : using Taguchi methods in technology and product development", *Addison-Wesley Publ. Co.*, 1995.

Goldenblum, A. A. Oprea, and V. Bogatu, "Time behavior of currents in ZnS:Mn metal-insulator-semiconductor-insulator-metal structure", *Journal of Applied Physics*, **75**, 3593 (1994).

Howard, W. E. O. Sahni, and P. M. Alt, "A simple model for the hysteretic behavior of ZnS:Mn thin film electroluminescent devices", *Journal of Applied Physics*, **53**, 639 (1982).

Hurd, J. M. and C. N. King, "Physical and electrical characterization of co-deposited ZnS:Mn electroluminescent thin film structures", *Journal of Electronic Materials*, **8**, 879 (1979).

Inoguchi, T., M. Takeda, Y. Kakihara, Y. Nakata, and M. Yoshida, "Stable high luminance Thin-film electroluminescent", *Digest of 1974 SID International Symposium*, 84 (1974).

Jarem, J. M. and V. P. Singh, "A computationally simple model for hysteretic thin-film electroluminescent devices", *IEEE Transactions on Electron Devices*, **ED-35**, 1834 (1988).

Keir, P. D., "Modeling phosphor space charge in alternating-current thin-film electroluminescent devices", M.S. Thesis, Oregon State University, 1995.

Keir, P. D., W. M. Ang, and J. F. Wager, "Modeling space charge in alternating-current thin-film electroluminescent devices using a single-sheet charge model", *Journal of Applied Physics*, **78**, 4668 (1995).

Lu, X., M.S. Thesis, Oregon State University, 1999.

Migita, M., O. Kanehisa, M. Shiiki and H. Yamamoto, "The preparation of ZnS:Mn electroluminescent layers by MOCVD using new manganese sources", *Journal of Crystal Growth*, **93**, 686 (1988).

Mikami, A., K. Terada, K. Okibayachi, K. Tanaka, M. Yoshida and S. Nakajima, "Chemical vapor deposition of ZnS:Mn electroluminescent film in a low-pressure halogen transport system", *Journal of Crystal Growth*, **110**, 381 (1991).

Mikami, A. K. Terada, K. Okibayachi, K. Tanaka, M. Yoshida and S. Nakajima, "Aging characteristics of ZnS:Mn electroluminescent film grown by a chemical vapor deposition technique", *Journal of Applied Physics*, **72**, 773 (1992).

Miller, R. T., "Halide transport chemical vapor deposition reactor system for deposition of ZnS:Mn electroluminescent phosphors", M.S. Thesis, Oregon State University, 1995.

Neyts, K. A., D. Corlatan, P. De Visschere, and J. Van den Bossche, "Observation and simulation of space-charge effects and hysteresis in ZnS:Mn ac thin-film electroluminescent", *Journal of Applied Physics*, **75**, 5339 (1994).

Nire, T., A. Matsuno, A. Miyakoshi, and K. Ohmi, "ZnS:Mn electroluminescent thin films prepared by deposition under controlled sulfur vapor pressure", *Japanese Journal of Applied Physics*, **33**, 2605 (1994).

Ono, Y. A., "Electroluminescent Display", *World Scientific Publishing Co. Pte. Ltd.*, 1995.

Russ, M. J. and D. I. Kennedy, "The effects of double insulating layers on the electrolumescence of evaporated ZnS:Mn film", *Journal of Electrochemical Society*, **114**, 1066 (1967).

Shih, S., "Electrical characterization and aging studies of ALE ZnS:Mn ACTFEL devices with varying phosphor thicknesses", M.S. Thesis, Oregon State University, 1996.

Singh, V.P., Q. Xu; S. Krishna, D.C. Morton, "Evaluation of phosphor current and carrier multiplication in ZnS:Mn ACTFEL devices", *Electroluminescence. Proceedings of the Sixth International Workshop*, 47 (1992).

Smith, D. H., "Modeling A.C. Thin-Film Electroluminescent Devices", *Journal of Luminescence*, **23**, 209 (1981).

Suntola, T., "Atomic layer epitaxy", *Thin Solid Films*, **216**, 84 (1992).

Takeda, M., Y. Kanatani, H. Kishishita, and H. Ueda, "TFEL displays of commercial production version", *Proc. SPIE **386**, Advances in display Technology III*, 34 (1983).

Theis, D., H. Oppolzer, G. Ebbinghaus, and S. Schild, "Cross-sectional transmission electron microscopy of electroluminescent thin films fabricated by various deposition methods", *Journal of Crystal Growth*, **63**, 47 (1983).

Thuemler, R. L., "Characterization of alternating-current thin-film SrS:Ce electroluminescent devices", M.S. Thesis, Oregon State University, 1996.

Vlasenko, N.A. and Iu. A. Poplov, "Study of the electroluminescence of a sublimed ZnS-Mn phosphor", *Optics & Spectroscopy*, **8**, 39 (1960).

Xian, H., P. Benalloul, C. Barthou and J. Benoit, "Quantitative analyses and crystallographic studies of ZnS:Mn thin films prepared by r.f. magnetron reactive sputtering", *Thin Solid Films*, **248**, 193 (1994).

Yang, K.-W. C. and S. J. T. Owen, "Mechanisms of the negative-resistance characteristics in thin-film electroluminescent devices", *IEEE Transactions on Electron Devices*, **ED-30**, 452 (1983).

Ylilammi, M., "Analytical circuit model for thin film electroluminescent devices", *IEEE Transactions on Electron Devices*, **42**,1227 (1995).